



UNIVERSITY COLLEGE DUBLIN
MASTERS THESIS

The Dynamics of Burgers Equation

Enda Carroll
16203944

supervised by
Assoc. Prof. Edward Cox
Assoc. Prof. Miguel Bustamante

March 17, 2020

Contents

1	Introduction	2
2	Review	3
3	Burgers Equation	4
3.1	Derivation from an Ideal Gas Setting	4
3.2	Characteristics	7
3.3	Analytical Solution - Hopf-Cole Transformation	12
4	Numerical Solution	15
4.1	Crank Nicolson Differencing & Upwind Schemes	16
4.2	Results	19
5	Triad Phase Dynamics in Fourier Space	22
5.1	Fourier Space Systems	23
5.2	Energy Spectrum and Energy Flux	25
5.3	Results	31
6	Conclusion	36
Appendix		37
References		39

1 Introduction

In this paper we present an examination of the dynamics of Burgers' equation in one dimension. Burgers' equation was introduced as a toy model for hydrodynamics by Burgers, [4], in the hope that studying it would significantly contribute to the still open problem of turbulence. The equation in its standard form is the following parabolic equation

$$\frac{\partial u}{\partial t} + u \frac{\partial u}{\partial x} = \nu \frac{\partial^2 u}{\partial x^2}, \quad (1)$$

where $u(x, t)$ is the velocity field and ν is kinematic viscosity. The equation describes the nonlinear evolution in time of a wave through space under competing effects of nonlinear wave steepening and dissipation. When viscosity is ignored the equation, known as the inviscid Burgers equation, becomes hyperbolic.

Intrinsic to the dynamics of Burgers' equation are the development of discontinuities, known as shocks, in the velocity profile in finite time. This is a result of the nonlinear term ($u \frac{\partial u}{\partial x}$) causing a steepening of negative gradients in the wavefront. Once shocks materialize they persist in the system and never disappear, in the inviscid case, but they may merge to form larger shocks (larger jump discontinuities). In the presence of viscosity these shocks dissipate energy. It is these dynamical features that provide the main focus of this paper, particularly where shocks merge, where Buzzicotti, Murray, Biferale and Bustamante, [5], and Murray and Bustamante, [13], have shown that *triad phase* interactions in Fourier space play a key role in the energy dynamics between waves in lead up to such events.

The outline of the paper is as follows. In the first section, we give a brief review of the topic of Burgers turbulence, outline the motivation for studying Burgers' equation and its variants, its use as a sandbox problem for gaining insight into the open Navier-Stokes problem as well as an introduction into current research which we eventually address in the later half of this paper. In the second section we present a mathematical analysis of the dynamics of Burgers' equation, we provide a derivation in a gasdynamics/acoustics context, we study the formation of shocks for both the inviscid and viscous case as well as examining a linearly damped version before presenting a transformation of the equation resulting in an exact solution. We then proceed to numerically solve the Burgers' equation for various initial conditions through finite differencing techniques, complimenting our work in the preceding section. Next, we shift focus to analysing a periodically forced version of Burgers' equation in Fourier space, where current research will be presented and discussed as well as providing complementary visuals intended to give a deeper understanding of how triad phases organize in Burgers turbulence. Finally, we make closing remarks, before discussing possible further work.

2 Review

The study of the equation described in (1) originated in 1915 when Bateman, [1], first proposed it to describe a wave profile. Later in Fay, [9], it was shown that, in a finite amplitude acoustic framework, Burgers' equation had a Fourier series solution. However it has since been named after Johannes Martinus Burgers after he proposed it as a simplified version for Navier-Stokes turbulence [4]. Then Hopf, [11], and Cole, [7], discovered that the equation was integrable through a transformation to the heat equation. Interest in the equation seemed to cease for a time following this, as the Hopf-Cole discovery rendered the equation a poor model for turbulence as it fails to capture the chaotic nature of turbulence. It experienced a resurgence in popularity in the later half of the last century where study focused on the equation rooted in a stochastically forced setting.

Burgers' equation and its variants appear in a wide range of applications [2]. The stochastic version, known as the Kardar-Parisi-Zhang equation is used to describe random interface growth in physics [12]. It has particular application in traffic flow modelling, [6], as well as arising in other areas such as gas dynamics, acoustics and statistical physics. Being that it is the simplest nonlinear PDE, the equation has pedagogical benefit in introducing important topics such as travelling waves and shock formation.

In today's research, the equation is still used as a sandbox problem for testing and developing numerical and mathematical tools for tackling the more complicated cases of turbulence, like the open Navier-Stokes problem. In Buzzicotti et al., [5], an equation for the flux of energy in a Fourier transformed stochastically forced Burgers' system is derived, where triad phase interactions play a key role in the exchange of energy amongst modes (waves). Through numerical simulation it is shown that these triad phase interactions produce maximal energy transfers amongst modes towards small length scales. Upon studying the evolution of these triad phases, it was also shown that triad phases cluster in and around unstable fixed points of $\pi/2 + 2n\pi$, and that these features are lost when modes are artificially taken out of the system. Subsequent work in Murray and Bustamante, [13], have shown that these triad phases in the so called 'inertial range' (scales where the only dominant feature is the nonlinear term, i.e., away from the forcing and dissipation ranges) produce maximal energy exchange amongst modes when synchronized (when all triads are in and around the same value) and aligned (all triads are at $\pi/2 + 2n\pi$). They also show that these features are still present, albeit less pronounced, in a 'phase-only' model of Burgers' equation in Fourier space. They show that these intermittent events of alignment and synchronisation in Fourier space triads have a direct correlation to shock mergers in real space.

In the second half of this paper we discuss further the work outlined above, as well providing visuals to compliment these findings. But first we present some mathematical analysis into the dynamics of Burgers' equation in real space.

3 Burgers Equation

3.1 Derivation from an Ideal Gas Setting

In this section we outline a derivation for Burgers' equation from an ideal gas setting. We achieve this by analysing the behaviour of perturbations to a gas in equilibrium by seeking asymptotic solutions that describe the nonlinear evolution of an acoustic signal, where for small amplitudes, the nonlinear effects take place over a long scale.

We begin with the governing equations of a one dimensional gas flow

$$\frac{\partial \rho}{\partial t} + \rho \frac{\partial u}{\partial x} + u \frac{\partial \rho}{\partial x} = 0, \quad (2)$$

$$\rho \frac{\partial u}{\partial t} + \rho u \frac{\partial u}{\partial x} + \frac{\partial p}{\partial x} = \frac{4}{3} \mu \frac{\partial^2 u}{\partial x^2}, \quad (3)$$

where $\rho(x, t)$ is the gas density, $p(x, t)$ is the gas pressure, $u(x, t)$ is the wave velocity in the positive x -direction, and $\mu(x, t)$ is dynamic or shear viscosity. The equation in (2) is the conservation of mass or mass balance equation for a gas and (3) is the conservation of momentum equation where we have included an extra term on the right-hand-side to model the effect of viscosity. In addition to the two conservation equations above we also have $c^2 = \frac{\partial p}{\partial \rho}$, where c is the local sound speed. We solve these equations subject to the following perturbed state conditions

$$p = p_0 + \rho_0 c_0 U f(\theta), \quad \rho = \rho_0 + \rho_0 \frac{U}{c_0} f(\theta), \quad u = U f(\theta), \quad (4)$$

where p_0 is the pressure, ρ_0 is the density and c_0 is the local sound speed of the gas at equilibrium, with U the initial velocity scale with typical frequency ω and $\theta = \omega t - k_0 x$, where $k_0 = \omega/c_0$. We now define the dimensionless variables

$$\bar{u} = \frac{u}{U}, \quad \bar{p} = \frac{p - p_0}{\rho_0 c_0 U}, \quad \bar{\rho} = \frac{(\rho - \rho_0) c_0}{\rho_0 U}, \quad c_0^2 = \frac{\gamma p_0}{\rho_0}, \quad (5)$$

with dimensionless time and space variables $\bar{x} = k_0 x$ and $\bar{t} = \omega t$, where γ is the specific heat ratio of an ideal gas. Substituting these into our equations of motion we find

$$\frac{\partial \bar{\rho}}{\partial \bar{t}} + \frac{\partial \bar{u}}{\partial \bar{x}} + M \frac{\partial \bar{\rho} \bar{u}}{\partial \bar{x}} = 0, \quad (6)$$

$$\left(\frac{\partial \bar{u}}{\partial \bar{t}} + M \bar{u} \frac{\partial \bar{u}}{\partial \bar{x}} \right) (1 + M \bar{\rho}) + \frac{\partial \bar{p}}{\partial \bar{x}} = \beta M \frac{\partial^2 \bar{u}}{\partial \bar{x}^2}, \quad (7)$$

$$1 + \gamma M \bar{p} = (1 + M \bar{\rho})^\gamma. \quad (8)$$

where $M = U/c_0$, $\beta M = 4\mu k_0/3\rho_0 c_0$ and we have used the equation of state, $p/p_0 = (\rho/\rho_0)^\gamma$, to arrive at (8). To investigate the behaviour of our gas as a result of perturbations to its equilibrium we now look for asymptotic expansions of the independent variables as $M \rightarrow 0$. However, a naive approximation of u will lead to solution only valid in a restricted range i.e., $0 \leq x \leq A$, for some $A < \infty$, as a result of variables evolving at different scales. Outside of this range we experience unbounded growth in our solution as result of a *secular* Mx term in the estimate. Therefore to acquire an approximation uniformly valid for $0 \leq x < \infty$, we use the *method of multiple scales*. We introduce a new slow changing variable $X = X(x) = Mx$, such that $u(x, t) \rightarrow u(x, X, t)$. Adjustment is required to our nondimensional equations, we replace $\frac{\partial}{\partial x} \rightarrow \frac{\partial}{\partial x} + M \frac{\partial}{\partial X}$ (note we will not need to replace the second order derivative as this will be absorbed into the high order expansion terms later) and we find

$$\frac{\partial \rho}{\partial t} + \frac{\partial u}{\partial x} + M \frac{\partial u}{\partial X} + M \frac{\partial \rho u}{\partial x} + M^2 \frac{\partial \rho u}{\partial X} = 0, \quad (9)$$

$$\left(\frac{\partial u}{\partial t} + M u \frac{\partial u}{\partial x} + M^2 u \frac{\partial u}{\partial X} \right) (1 + M \rho) + \frac{\partial p}{\partial x} + M \frac{\partial p}{\partial X} = \beta M \frac{\partial^2 u}{\partial x^2}, \quad (10)$$

$$1 + \gamma M p = (1 + M \rho)^\gamma. \quad (11)$$

where we have dropped the bar notation for convenience. We are now ready to look for asymptotic approximations for our independent variables

$$\begin{aligned} u(x, X, t) &= u_0(x, X, t) + M u_1(x, X, t) + \mathcal{O}(M^2), \\ p(x, X, t) &= p_0(x, X, t) + M p_1(x, X, t) + \mathcal{O}(M^2), \\ \rho(x, X, t) &= \rho_0(x, X, t) + M \rho_1(x, X, t) + \mathcal{O}(M^2), \end{aligned} \quad (12)$$

with the added requirement that the expansions be asymptotic for $t = \mathcal{O}(1)$ and $0 \leq x \leq \mathcal{O}(M^{-1})$ as $M \rightarrow 0$. Replacing the variables in our nondimensional equations with these approximations we find

$$\frac{\partial \rho_0}{\partial t} + \frac{\partial u_0}{\partial x} + M \left(\frac{\partial \rho_1}{\partial t} + \frac{\partial u_1}{\partial x} + \frac{\partial u_0}{\partial X} + \frac{\partial \rho_0 u_0}{\partial x} \right) + \mathcal{O}(M^2) = 0, \quad (13)$$

$$\frac{\partial u_0}{\partial t} + \frac{\partial p_0}{\partial x} + M \left(\frac{\partial u_1}{\partial t} + \frac{\partial p_1}{\partial x} + \rho_0 \frac{\partial u_0}{\partial x} + u_0 \frac{\partial u_0}{\partial x} + \frac{\partial p_0}{\partial X} - \beta \frac{\partial^2 u_0}{\partial x^2} \right) + \mathcal{O}(M^2) = 0, \quad (14)$$

$$p_0 - \rho_0 + M \left(p_1 - \rho_1 - \frac{\gamma-1}{2} \rho_0^2 \right) + \mathcal{O}(M^2) = 0, \quad (15)$$

where we have taken the expansion of the right-hand-side of (11), $(1 + M\rho)^\gamma = 1 + \gamma M\rho + \frac{\gamma(\gamma-1)}{2} M^2 \rho^2 + \dots$, to arrive at (15). Ignoring higher order terms and matching terms of $\mathcal{O}(1)$ and $\mathcal{O}(M)$ we find the following systems of equations

$$\mathcal{O}(1) \Rightarrow \begin{cases} \frac{\partial \rho_0}{\partial t} + \frac{\partial u_0}{\partial x} = 0, \\ \frac{\partial u_0}{\partial t} + \frac{\partial p_0}{\partial x} = 0, \\ p_0 = \rho_0, \end{cases} \quad (16)$$

and

$$\mathcal{O}(M) \Rightarrow \begin{cases} \frac{\partial \rho_1}{\partial t} + \frac{\partial u_1}{\partial x} = -\frac{\partial}{\partial x}(\rho_0 u_0) - \frac{\partial u_0}{\partial X}, \\ \frac{\partial u_1}{\partial t} + \frac{\partial p_1}{\partial x} = -\rho_0 \frac{\partial u_0}{\partial t} - u_0 \frac{\partial u_0}{\partial x} - \frac{\partial p_0}{\partial X} + \beta \frac{\partial^2 u_0}{\partial x^2}, \\ p_1 = \rho_1 + \frac{\gamma-1}{2} \rho_0^2. \end{cases} \quad (17)$$

Concerning ourselves with solving the $\mathcal{O}(1)$ system initially, we notice that (16) can be rewritten as the linear wave equation in any of the variables u_0 , p_0 or ρ_0 i.e.,

$$\left(\frac{\partial^2}{\partial t^2} - \frac{\partial^2}{\partial x^2} \right) (u_0, p_0, \rho_0) = 0. \quad (18)$$

As we are concerned with the propagation of a wave in the positive x-direction we may only consider the right running wave in D'Alembert's solution to the wave equation. We therefore find the solutions to the $\mathcal{O}(1)$ system

$$u_0 = p_0 = \rho_0 = q(\theta, X), \quad \theta = t - x, \quad (19)$$

for an arbitrary function q . Notice that, although not explicitly stated in the system, our solution is dependant on X as we have embedded the problem in this higher dimension. Substituting these solutions into the $\mathcal{O}(M)$ system we find after a little manipulation

$$\left(\frac{\partial^2}{\partial t^2} - \frac{\partial^2}{\partial x^2} \right) u_0 = -\frac{\gamma-1}{2} \frac{\partial^2 q^2}{\partial t^2} + \frac{\partial^2 q^2}{\partial x^2} + \frac{\partial q}{\partial x \partial X} - \frac{\partial q}{\partial t \partial X} + \beta \frac{\partial q}{\partial t \partial x^2} \quad (20)$$

where we are now focused on the solution for u_1 only. We can replace the derivatives in x and t on the right-hand-side with appropriate derivatives of θ by recalling $\theta = t - x$ to find

$$\left(\frac{\partial^2}{\partial t^2} - \frac{\partial^2}{\partial x^2} \right) u_0 = \frac{\gamma+1}{2} \frac{\partial^2 q^2}{\partial \theta^2} - 2 \frac{\partial q}{\partial \theta \partial X} + \beta \frac{\partial^3 q}{\partial \theta^3}. \quad (21)$$

The theory of multiple scales states that to avoid any unbounded growth in our solution we must impose solubility conditions on the secular terms. Since the right-hand-side resonates on fast scales we set this to be zero

$$\begin{aligned} \frac{\gamma+1}{2} \frac{\partial^2 q^2}{\partial \theta^2} - 2 \frac{\partial q}{\partial \theta \partial X} + \beta \frac{\partial^3 q}{\partial \theta^3} &= 0, \\ \frac{\partial}{\partial \theta} \left(\frac{\gamma+1}{2} \frac{\partial q^2}{\partial \theta} - 2 \frac{\partial q}{\partial X} + \beta \frac{\partial^2 q}{\partial \theta^2} \right) &= 0, \\ \frac{2}{\gamma+1} \frac{\partial q}{\partial X} - q \frac{\partial q}{\partial \theta} &= \frac{\beta}{\gamma+1} \frac{\partial^2 q}{\partial \theta^2}. \end{aligned} \quad (22)$$

Finally, we define the variable $Z = \frac{\gamma+1}{2}X$ and let $\epsilon = \frac{\beta}{\gamma+1}$, substituting these into (22) above we get

$$\frac{\partial q}{\partial Z} - q \frac{\partial q}{\partial \theta} = \epsilon \frac{\partial^2 q}{\partial \theta^2}. \quad (23)$$

Which is Burgers' equation, written in the form appropriate for a signalling problem, where Z can be seen as a time-like variable and θ a space-like variable for appropriate initial conditions.

3.2 Characteristics

Here we construct solutions of the inviscid Burgers equation. We then analyse the formation of discontinuities in the wave profile of (1). This is achieved by examining the characteristic curves of the inviscid Burgers equation using the method of characteristics. We will see that the nonlinear evolution of the wave profile can lead to unphysical behaviour in finite time resulting in regions where the solution becomes multivalued. We also consider a linearly damped version of the inviscid Burgers' equation and investigate how damping of the wave can prevent shock formation.

The method of characteristics transforms a PDE to a system of ODEs that lie on curves in the solution space that can be solved for and transformed back into a solution for the

original PDE. The method enables us to obtain qualitative information on the solution structure of the PDE for example shock formation. The direction of the characteristic curves indicate the flow of values through the solution. This is useful when solving PDEs numerically as it can indicate which finite difference scheme is best for the problem.

Consider the inviscid Burgers equation with some initial wave profile

$$\frac{\partial u}{\partial t} + u \frac{\partial u}{\partial x} = 0, \quad (24)$$

$$u(x, 0) = F(x). \quad (25)$$

We reparameterize such that $x = x(r, \alpha)$, $t = t(r, \alpha)$, $u = u(r, \alpha)$, where r determines where on the characteristic we lie and α is the x -position at $t = 0$ i.e., the point on the initial curve. Thus the system of ODEs are as follows

$$\frac{\partial x}{\partial r} = u, \quad \frac{\partial t}{\partial r} = 1, \quad \frac{\partial u}{\partial r} = 0, \quad (26)$$

we are free to choose the value of r at $t = 0$, so for convenience we choose $r = 0$. Therefore the corresponding initial conditions are $x(0, \alpha) = \alpha$, $t(0, \alpha) = 0$ and $u(0, \alpha) = F(\alpha)$. Solving the system subject to these initial conditions we find a family of characteristic curves

$$\begin{aligned} u(x, t) &= F(\alpha), \\ t &= r, \\ x &= F(\alpha)t + \alpha, \end{aligned} \quad (27)$$

and the solution of $u(x, t)$ is

$$\left. \begin{aligned} u(x, t) &= F(\alpha), \\ \alpha &= x - F(\alpha)t \end{aligned} \right\} \quad (28)$$

We can see from the equation in (27) that the characteristics are straight lines emanating from $(\alpha, 0)$ with speed $u = F(\alpha)$. Therefore the larger $F(\alpha)$, the faster the wave travels and the more horizontal the characteristic curve becomes. The characteristics also have a constant slope of $1/F(\alpha)$ but these slopes are dependent on which characteristic one is on. This leads eventually to the crossing of characteristics in finite time and generating multivalued regions in (x, t) space. These multivalued regions are unphysical and can be replaced by single valued regions where characteristics intersect on a curve known as the shock curve. We can find the time and position, t_s and x_s , of when the shock first forms

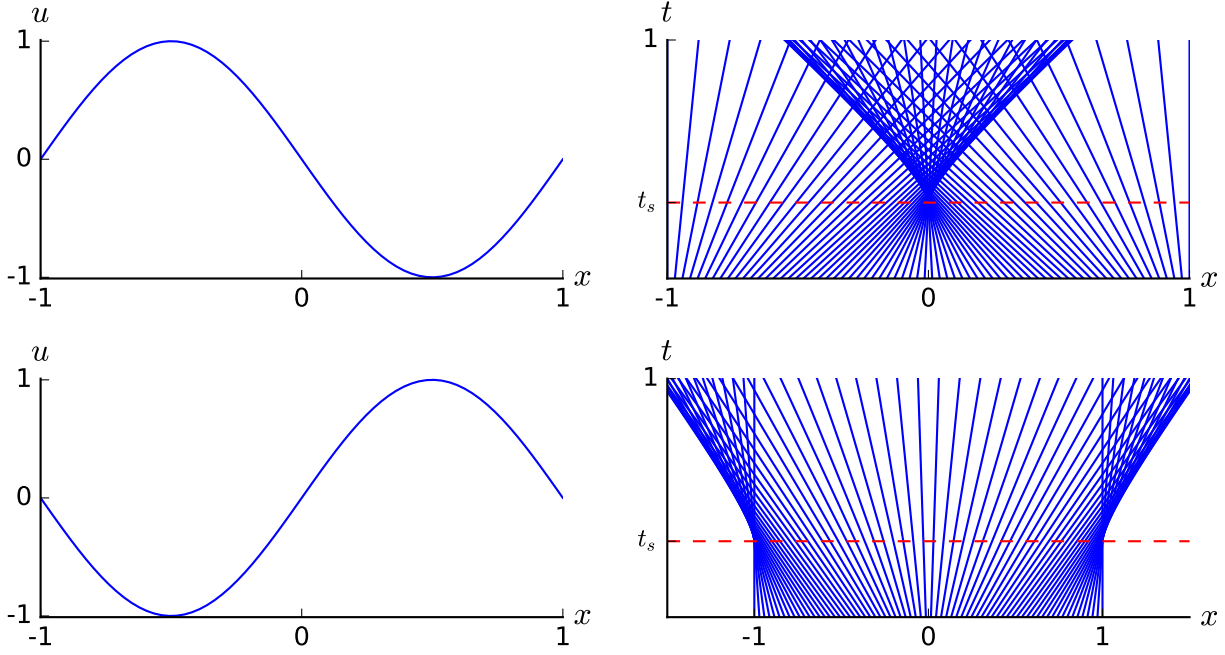


Figure 1: Initial wave profile (left) and corresponding characteristic curves (right) for the inviscid Burgers' equation with initial conditions $u(x, 0) = -\sin(\pi x)$ (top) and $u(x, 0) = \sin(\pi x)$ (bottom).

by considering two neighbouring characteristics, α and $\alpha + \Delta\alpha$ which intersect at time t_s . Then to find t_s we simply take the derivative of (27) with respect to α and solve

$$\begin{aligned} \frac{\partial x}{\partial \alpha} &= F'(\alpha)t_s + 1 = 0 \\ t_s &= -\frac{1}{F'(\alpha)} \end{aligned} \tag{29}$$

or to be more precise, the time of the first shock is

$$t_s = -\frac{1}{\min \{F'(\alpha)\}} \tag{30}$$

We can simply substitute t_s back into (27) and any value of α where $F'(\alpha) = \min \{F'(\alpha)\}$ to find x_s .

In figure 1, the characteristics of Burgers' equation for sinusoidal initial conditions are shown as well as the corresponding initial wave profiles. The top left panel displays initial conditions of a shifted sin wave i.e., $u(x, 0) = -\sin(\pi x)$. The top right panels shows the

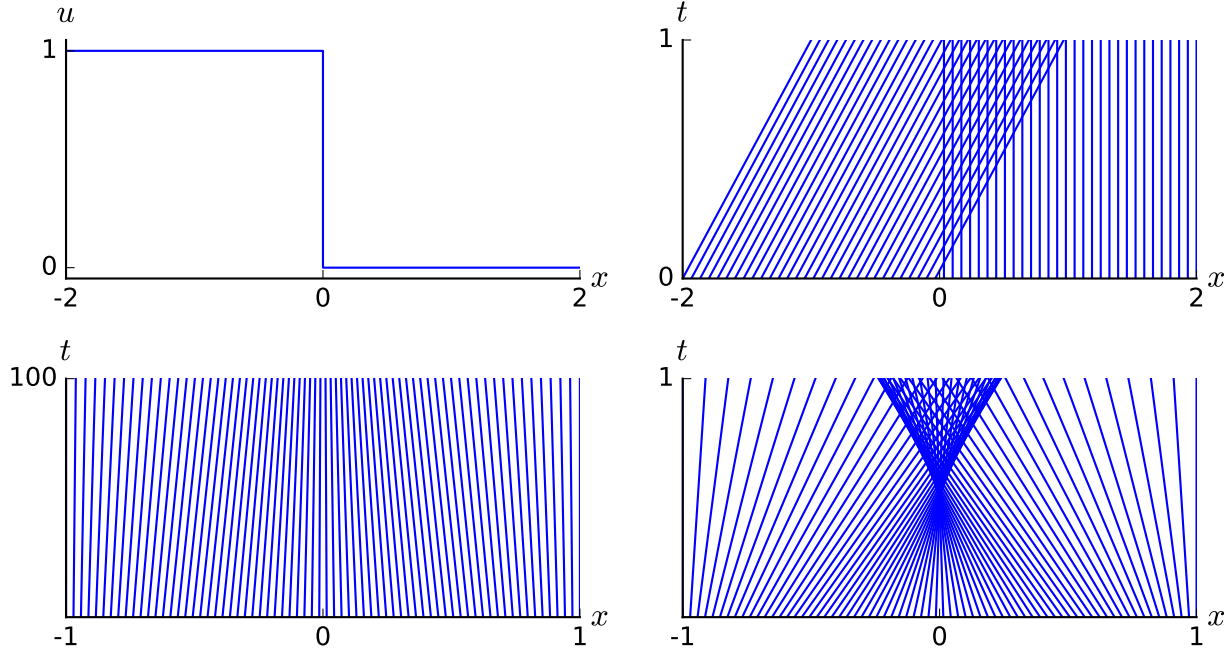


Figure 2: (Top) Initial wave profile (left) and corresponding characteristic curves (right) for the inviscid Burgers' equation with Riemann type initial conditions. (Bottom)

corresponding characteristics. We see that for $u > 0$ i.e., parts of the wave above the x -axis, the corresponding characteristics have positive slope and therefore flow forward. The characteristics corresponding to $u < 0$ have negative slope and flow in the negative x direction. We also see that for parts of the wave where u is largest (either positive or negative) the slope of the characteristics is most severe. The positive parts of the wave flow forward and the negative backward until a shock forms at $t_s = -1 / \min \{-\pi \cos(\pi \alpha)\} = 1/\pi$ and $x_s = 0$ as seen in the top right panel. Similarly, in the bottom left panel initial conditions corresponding to $u(x, 0) = \sin(\pi x)$ are shown. This time the wavefronts are flowing away from each other and instead of one shock formation at $t_s = 1/\pi$ we have two shocks forming at $x_s = \pm 1$.

In the top two panels of figure 2 we have a special case of initial waveform. This initial waveform, also known as the Riemann problem, is an extreme case of initial wave profile and can be expressed as follows

$$u(x, 0) = \begin{cases} u_l & x \leq 0 \\ u_r & x \geq 0 \end{cases} \quad (31)$$

with the additional condition that $u_l > u_r$, where in figure 2 we have chosen $u_l = 1$ and $u_r = 0$. These initial conditions describe a wave with immediate shock formation which is

apparent from the plot of the characteristics in the top right panel. We use these initial conditions in section 4 to obtain an analytical solution to compare our numerical estimates against.

To investigate the effect of damping on the formation of shocks we consider a damped version of the inviscid Burgers equation with some initial wave profile

$$\frac{\partial u}{\partial t} + u \frac{\partial u}{\partial x} + \lambda u = 0, \quad (32)$$

$$u(x, 0) = F(x). \quad (33)$$

for $\lambda > 0$. The reparameterized characteristic system is

$$\frac{\partial x}{\partial r} = u, \quad \frac{\partial t}{\partial r} = 1, \quad \frac{\partial u}{\partial r} = \lambda u. \quad (34)$$

Solving this system we find

$$x = \alpha + F(\alpha) \left(\frac{1 - e^{-\lambda t}}{\lambda} \right), \quad (35)$$

and the characteristic solution to (33) is

$$\left. \begin{aligned} u(x, t) &= F(\alpha), \\ \alpha &= x - F(\alpha) \left(\frac{1 - e^{-\lambda t}}{\lambda} \right) \end{aligned} \right\} \quad (36)$$

To find the conditions necessary for shock formation, we consider again two neighbouring characteristic curves that intersect. However we now suppose shock formation occurs at $t_s \rightarrow \infty$, this allows us to extract the formation condition on λ . The characteristics intersect when

$$\frac{\partial x}{\partial \alpha} = 1 + F'(\alpha) \left(\frac{1 - e^{-\lambda t_s}}{\lambda} \right) = 0 \quad (37)$$

and since $\lambda > 0$, the derivative is zero if and only if

$$F'(\alpha) < -\lambda \quad (38)$$

The condition above would suggest that in order for a shock to form the gradient of the initial wavefront needs to be sufficiently severe to overcome the effect of damping. In other

words the damping term counteracts the effect the nonlinear term has at distorting the wave profile and, depending on the value of λ , has the ability to suppress wave distortion (shock formation) entirely. In the bottom panels of figure 2 the characteristics of the of Burgers' equation with $u(x, 0) = -\sin(\pi x)$ for two values of λ . The left panel shows the characteristic curves for $\lambda = 10$. We see that even for sufficiently long time the characteristics do not cross and no shock forms. In contrast, the bottom right panel shows characteristics for $\lambda = 0.9$ with evident shock formation. Even though there is damping in the system a shock still develops, albeit at an apparently later time.

In the examples presented above we have seen how and when shocks form in the solutions to Burgers' equation. They arise when the solution becomes multivalued or, as we have seen above, when characteristic curves intersect. We have not discussed, however, how to deal with such scenarios in construction of a valid solution. This requires some mathematical extension of what we mean by a solution since strictly speaking the derivatives of u will not exist at a discontinuity. It can be done through the concept of a *weak* solution. However, by expanding our class of solutions to include discontinuous solutions, we can no longer guarantee the uniqueness of the solution. The nonuniqueness can be resolved by appealing to physically inspired criteria, for example viscosity ($\nu \frac{\partial^2 u}{\partial x^2}$). In the next section we discuss a transformation of the full Burgers equation resulting in an exact solution.

3.3 Analytical Solution - Hopf-Cole Transformation

The non-linearity of Burgers' equation means that finding a general solution is non-trivial and in most cases we are restricted to solving it numerically. However for special cases one can obtain explicit solutions, like in Hopf, [11], and Cole, [7], where it was proposed that under a nonlinear transformation of the dependant variable one can map (1) to the linear diffusion equation for which there exists a closed analytical solution. Here we outline this mechanism, now known as the Hopf-Cole transformation, for finding an explicit solution to Burgers' equation. This solution is then used in the subsequent section as a reference for our numerical analysis.

The transformation maps $u(x, t)$ to $\phi(x, t)$ under the following,

$$u = -2\nu \frac{\partial \ln \phi}{\partial x} = -2\nu \frac{\phi_x}{\phi}, \quad (39)$$

where ϕ_x denotes the derivative with respect to x . We define the variable $\psi = -2\nu \ln(\phi)$, where $u = \psi_x$ and substituting this into (1) we find

$$\begin{aligned}
\psi_{xt} + \psi_x \psi_{xx} &= \nu \psi_{xxx}, \\
\frac{\partial}{\partial \theta} \left(\psi_t + \frac{1}{2} \psi_x^2 - \nu \psi_{xx} \right) &= 0, \\
\psi_t + \frac{1}{2} \psi_x^2 - \nu \psi_{xx} &= 0.
\end{aligned} \tag{40}$$

Substituting back in the definition for ψ we find

$$\begin{aligned}
-2\nu \frac{\phi_t}{\phi} + \frac{1}{2} 4\nu^2 \left(\frac{\phi_x}{\phi} \right)^2 &= \nu \left(-2\nu \left(\frac{\phi_{xx}}{\phi} - \left(\frac{\phi_x}{\phi} \right)^2 \right) \right), \\
-2\nu \frac{\phi_t}{\phi} &= -2\nu^2 \frac{\phi_{xx}}{\phi}, \\
\phi_t &= \nu \phi_{xx}.
\end{aligned} \tag{41}$$

This is the equation for diffusion of heat through a medium or simply the heat equation which is of course linear in $\phi(x, t)$. The general solution for (41) is well known and takes the form

$$\phi(x, t) = \int_{-\infty}^{\infty} \Phi(x - y, t) g(y) dy, \tag{42}$$

where $\Phi(x, t) = \frac{1}{\sqrt{4\pi\nu t}} e^{-\frac{x^2}{4\nu t}}$ is the fundamental solution, also known as the heat kernel and $g(x)$ satisfies the initial condition $\phi(x, 0) = g(x)$. Recalling our transformation on $u(x, t)$, we find the transformed initial conditions for (41)

$$\phi(x, 0) = \phi_0(x) = e^{-\frac{1}{2\nu} \int_0^x u_0(s) ds}. \tag{43}$$

where $u_0(x) = u(x, 0)$. Therefore the solution to (41) subject to the initial conditions above is

$$\phi(x, t) = \frac{1}{\sqrt{4\pi\nu t}} \int_{-\infty}^{\infty} e^{-\frac{G(x, y, t)}{2\nu}} dy, \tag{44}$$

where $G(x, y, t) = \frac{(x-y)^2}{2t} + \int_0^y u_0(s) ds$. Mapping this solution back to the Burgers equation we find the following general solution

$$u(x, t) = -2\nu \frac{\phi_x}{\phi} = \frac{\int_{-\infty}^{\infty} \left(\frac{x-y}{t} \right) e^{-\frac{G(x, y, t)}{2\nu}} dy}{\int_{-\infty}^{\infty} e^{-\frac{G(x, y, t)}{2\nu}} dy}. \tag{45}$$

The solution above is continuous and single valued and for all values of t . It is very hard to give a physical interpretation of this exact solution unless a suitable simple form of $g(x)$ is specified. In the next section where we numerically solve (1), the exact solution in (45) provides a benchmark for which we can compare our numerical estimates to.

In most cases an exact expression for the integrals in (45) are difficult to obtain. However, they can be asymptotically estimated in the limit of vanishing viscosity using Laplace's method [14]. As $\nu \rightarrow 0$, with x and t fixed, we find an estimation for the integrals above by noticing that the dominant contributions to the integrals come from the neighbourhood of the stationary points of $G(x, y, t)$, or more specifically the local maxima of $-G(x, y, t)$. Then using a Taylor series expansion of G we obtain an asymptotic approximation to (45).

The stationary points of $G(x, y, t)$ occur when

$$\frac{\partial G}{\partial y} = -\left(\frac{x-y}{t}\right) + u_0(y) = 0, \quad (46)$$

solving for y we find the stationary point of G . Let $y = y_0$ be the stationary point of G , substituting into (46) above we find

$$x = y_0 + u_0(y_0)t, \quad (47)$$

which is the characteristic equation for the inviscid case of Burgers' equation we found in the previous section. The stationary point, y_0 , is a maximum if

$$\frac{\partial^2 G}{\partial y^2} = \frac{1}{t} + u_0'(y) > 0, \quad (48)$$

which is satisfied if $u_0'(y_0) > 0$ or for times $t < \frac{-1}{c_0'(y_0)}$, which corresponds to times up to and before shock formation. If this is the case and there is only one such y_0 , then we are in a region where the solution is single valued and y_0 is a global maximum. In the neighbourhood of this maximum we find an asymptotic expansion of G as

$$G(x, y, t) = G(x, y_0, t) + \frac{1}{2}(y - y_0)^2 \left[\frac{1}{t} + u_0'(y) \right] + \mathcal{O}((y - y_0)^3). \quad (49)$$

Ignoring higher order terms, multiplying both sides by $-1/2\nu$, taking the exponential and integrating we find

$$\int_{-\infty}^{\infty} e^{-\frac{G(x, y, t)}{2\nu}} dy \approx e^{-\frac{G(x, y_0, t)}{2\nu}} \int_{-\infty}^{\infty} e^{-\frac{(y-y_0)^2 \left[\frac{1}{t} + u_0'(y) \right]}{4\nu}} dy, \quad (50)$$

$$= e^{-\frac{G(x, y_0, t)}{2\nu}} \sqrt{\frac{4\pi\nu}{\left(\frac{1}{t} + u_0'(y) \right)}}, \quad (51)$$

where the integral on the right hand side of (50) is the Gaussian integral. Similarly we find the asymptotic estimation for the integral in the denominator of (45) as

$$\int_{-\infty}^{\infty} \left(\frac{x-y}{t} \right) e^{-\frac{G(x,y,t)}{2\nu}} dy \approx \left(\frac{x-y_0}{t} \right) e^{-\frac{G(x,y_0,t)}{2\nu}} \sqrt{\frac{4\pi\nu}{\left(\frac{1}{t} + u'_0(y) \right)}}. \quad (52)$$

Finally substituting these expressions back into (45) we are left with

$$u(x, t) \approx \left(\frac{x-y_0}{t} \right) = u_0(y_0). \quad (53)$$

Thus for a single valued characteristic passing through a given point (x, t) the asymptotic solution to the viscous Burgers equation can be summarized by

$$\left. \begin{aligned} u(x, t) &= u_0(y_0), \\ y_0 &= x - u_0(y_0)t. \end{aligned} \right\} \quad (54)$$

which is identical to the characteristic based solution for the inviscid Burgers case we have seen in the previous section. Although the exact solution of Burgers' equation is a single valued and continuous function for all time t , the asymptotic solution (54) exhibits instability. It has already been shown that this progressively distorts itself and becomes multiple-valued after sufficiently long time i.e., for $t > t_s$. Eventually, the wave would break with the formation of a discontinuity as a shock wave. When this state is reached, there will be two stationary points of (46), thus, further application of Laplace's method is required to complete the asymptotic analysis (see [3]).

4 Numerical Solution

As a result of the non-linearity of Burgers' equation, a general exact solution does not exist and we are therefore forced to solve it numerically. Previously we outlined a transformation of the viscous case of Burgers' equation to obtain an exact solution. This solution is only valid for certain initial condition, however, it is useful for testing the accuracy of numerical schemes designed to solve Burgers' equation. In this section we use results from previous sections including the characteristic solutions in section 2.3 as an aid to numerically solving Burgers' equation. We make use of finite differencing schemes in particular Crank-Nicolson and upwind differencing. The Crank-Nicolson approach to differencing produces an implicit

system of linear equations. The resulting system is converted into a banded matrix form and then solved. We utilize the Thomas algorithm (see appendix), which takes advantage of the banded nature of the system and greatly improves the efficiency of our numerical scheme. The scheme is then used to solve the viscous Burgers equation for various initial conditions.

Throughout this section we refer to Burgers' equation in conservative form,

$$\frac{\partial u}{\partial t} + \frac{\partial F}{\partial x} - \nu \frac{\partial^2 u}{\partial x^2} = 0, \quad (55)$$

where $F = \frac{u^2}{2}$.

4.1 Crank Nicolson Differencing & Upwind Schemes

In order to solve for $u(x, t)$ in (55) numerically we switch from the continuous (x, t) space to a 2-D discretized grid with equidistant grid points. Each grid point is separated by an arbitrary step size, Δx in the x -direction and Δt in the t -direction, such that

$$\begin{aligned} x_j &= x_0 + j\Delta x & j &= 1, 2, \dots, J, \\ t_n &= t_0 + n\Delta t & n &= 1, 2, \dots, N, \end{aligned} \quad (56)$$

is a complete description of the grid space for some initial x_0 and t_0 . Therefore the solution of $u(x, t)$ is approximated by $u(x_j, t_n) \equiv U_j^n$, where U_j^n denotes the estimate at the j^{th} spatial grid point and n^{th} temporal grid point. In finite differencing schemes one approximates derivatives of u in terms of U_j^n by taking a Taylor series expansion and making appropriate truncations. This can be achieved for any order of derivative. In this paper we employ Crank-Nicolson differencing to approximate the derivatives in (55). Crank-Nicolson methods take a combination of a forward differencing at the n^{th} time step and a backward differencing at the $n + 1^{th}$ time step. Therefore the time derivative is approximated by a simple forward in time difference

$$\frac{\partial u}{\partial t} \approx \frac{U_j^{n+1} - U_j^n}{\Delta t}, \quad (57)$$

and the dissipation term as

$$\nu \frac{\partial^2 u}{\partial x^2} \approx \nu \frac{(U_{j-1}^n - 2U_j^n + U_{j+1}^n) + (U_{j-1}^{n+1} - 2U_j^{n+1} + U_{j+1}^{n+1})}{2\Delta x^2} \equiv \frac{\nu L_{xx}(U_j^n + U_j^{n+1})}{2}, \quad (58)$$

where we use the $L_{xx}()$ operator to denote second order centred spatial differencing. The nonlinear term is

$$\frac{\partial F}{\partial x} \approx \frac{(F_{j+1}^n - F_{j-1}^n) + (F_{j+1}^{n+1} - F_{j-1}^{n+1})}{4\Delta x} \equiv \frac{L_x(F_j^n + F_j^{n+1})}{2}, \quad (59)$$

where $L_x()$ denotes first order centred spatial differencing. In order to produce a system of linear equations we make an approximation of the nonlinear term. To achieve this we take a Taylor series expansion of F_j^{n+1} about the n^{th} time step such that

$$F_j^{n+1} = F_j^n + \Delta t \left[\frac{\partial F}{\partial t} \right]_j^n + \mathcal{O}(\Delta t^2). \quad (60)$$

The first derivative term can be rewritten as

$$\left[\frac{\partial F}{\partial t} \right]_j^n = \left[\frac{\partial U}{\partial t} \frac{\partial F}{\partial U} \right]_j^n = \left[\frac{\partial U}{\partial t} \right]_j^n \left[\frac{\partial F}{\partial U} \right]_j^n = \frac{U_j^{n+1} - U_j^n}{\Delta t} U_j^n, \quad (61)$$

ignoring higher order terms and substituting this expansion back into (58) we find

$$\begin{aligned} \frac{L_x(F_j^n + F_j^{n+1})}{2} &= \frac{L_x(2F_j^n + U_j^n(U_j^{n+1} - U_j^{n-1}))}{2} \\ &= \frac{L_x(2 \left[\frac{U^2}{2} \right]_j^n) + L_x(U_j^n U_j^{n+1}) - L_x(U_j^n U_j^n)}{2} \\ &= \frac{L_x(U_j^n U_j^{n+1})}{2} \end{aligned} \quad (62)$$

We now have a finite difference scheme that can be implemented to solve (55) numerically. However, we can improve on the scheme outlined above. Since we are considering the propagation of a wave, we can make use of the information from the characteristics we found in section 2.3. This is accomplished by including more spatial nodes in the first order operator above. This approach is known as upwind differencing and was first introduced by Courant, Issacson and Rees, [8]. Upwind differencing is determined by information *upwind* of node (j, n) , the direction of which, is dependant on the slope of the characteristics. Explicitly, $L_x() \rightarrow L_x^4()$ where $L_x^4(U_j^n)$ is defined as

$$L_x^4(U_j^n) = \begin{cases} \frac{U_{j+1}^n - U_{j-1}^n}{2\Delta x} + \frac{U_{j-2}^n - 3U_{j-1}^n + 3U_j^n - U_{j+1}^n}{6\Delta x} & U_j^n > 0, \\ \frac{U_{j+1}^n - U_{j-1}^n}{2\Delta x} + \frac{U_{j-1}^n - 3U_j^n + 3U_{j+1}^n - U_{j+2}^n}{6\Delta x} & U_j^n < 0, \end{cases} \quad (63)$$

this is known as four point upwind differencing, as we are using four spatial grid points. Our difference scheme can now be written as

$$\frac{U_j^{n+1} - U_j^n}{\Delta t} = -\frac{L_x^4(U_j^n U_j^{n+1})}{2} + \frac{\nu L_{xx}(U_j^n + U_j^{n+1})}{2}, \quad (64)$$

and with a little manipulation this can be expressed as a quadridiagonal system of linear equations

$$e_j^n U_{j-2}^{n+1} + a_j^n U_{j-1}^{n+1} + b_j^n U_j^{n+1} + c_j^n U_{j+1}^{n+1} = d_j^n \quad U_j^n > 0, \quad (65)$$

$$a_j^n U_{j-1}^{n+1} + b_j^n U_j^{n+1} + c_j^n U_{j+1}^{n+1} + f_j^n U_{j+2}^{n+1} = d_j^n \quad U_j^n < 0, \quad (66)$$

where for $U_j^n > 0$ we have

$$\begin{aligned} e_j^n &= \frac{\Delta t}{12\Delta x} U_{j-2}^n, \\ a_j^n &= -\frac{\Delta t}{2\Delta x} U_{j-1}^n - \nu \frac{\Delta t}{2\Delta x^2}, \\ b_j^n &= 1 + \frac{\Delta t}{4\Delta x} U_j^n + \nu \frac{\Delta t}{2\Delta x^2}, \\ c_j^n &= \frac{\Delta t}{3\Delta x} U_{j+1}^n - \nu \frac{\Delta t}{2\Delta x^2}, \\ d_j^n &= \nu \frac{\Delta t}{2\Delta x^2} U_{j-1}^n + \left(1 - \nu \frac{\Delta t}{2\Delta x^2}\right) U_j^n + \nu \frac{\Delta t}{2\Delta x^2} U_{j+1}^n, \end{aligned} \quad (67)$$

and for $U_j^n < 0$

$$\begin{aligned} a_j^n &= -\frac{\Delta t}{6\Delta x} U_{j-1}^n - \nu \frac{\Delta t}{2\Delta x^2}, \\ b_j^n &= 1 - \frac{\Delta t}{4\Delta x} U_j^n + \nu \frac{\Delta t}{2\Delta x^2}, \\ c_j^n &= \frac{\Delta t}{2\Delta x} U_{j+1}^n - \nu \frac{\Delta t}{2\Delta x^2}, \\ f_j^n &= -\frac{\Delta t}{12\Delta x} U_{j+2}^n, \end{aligned} \quad (68)$$

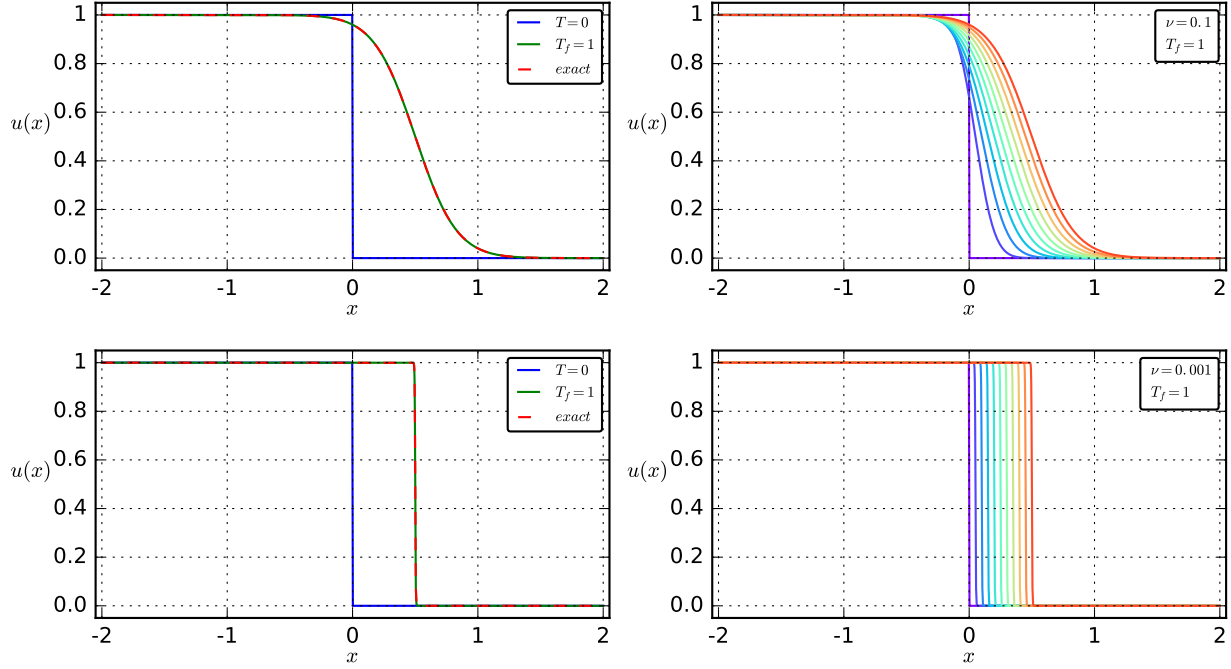


Figure 3: (Left) Simulation and exact results of Burgers' equation and (right) evolution of the wave profile subject to Reimann initial conditions for $\nu = 0.1$ (top) and $\nu = 0.001$ (bottom). Simulation was performed with 1600 steps ($\Delta x = 0.003$ and $\Delta t = 0.001$) and $T_f = 1.0$.

with d_j the same as in (67) above. In the next section the four point upwind scheme outlined above is implemented using the extended Thomas algorithm to solve (55) numerically for the various initial conditions that we have seen in section 2.3.

4.2 Results

In order to measure the effectiveness and accuracy of the numerical scheme we outlined in the previous section we make use of the exact solution we found using the Hopf-Cole transformation. We use the result in (45) subject to the Reimann initial conditions in (31) with $u_l = 1$ and $u_r = 0$ on the domain $-2 \leq x \leq 2$, (all simulations in this section are performed in this domain) with the following boundary conditions

$$u(-2, t) = 1, \quad u(2, t) = 0. \quad (69)$$

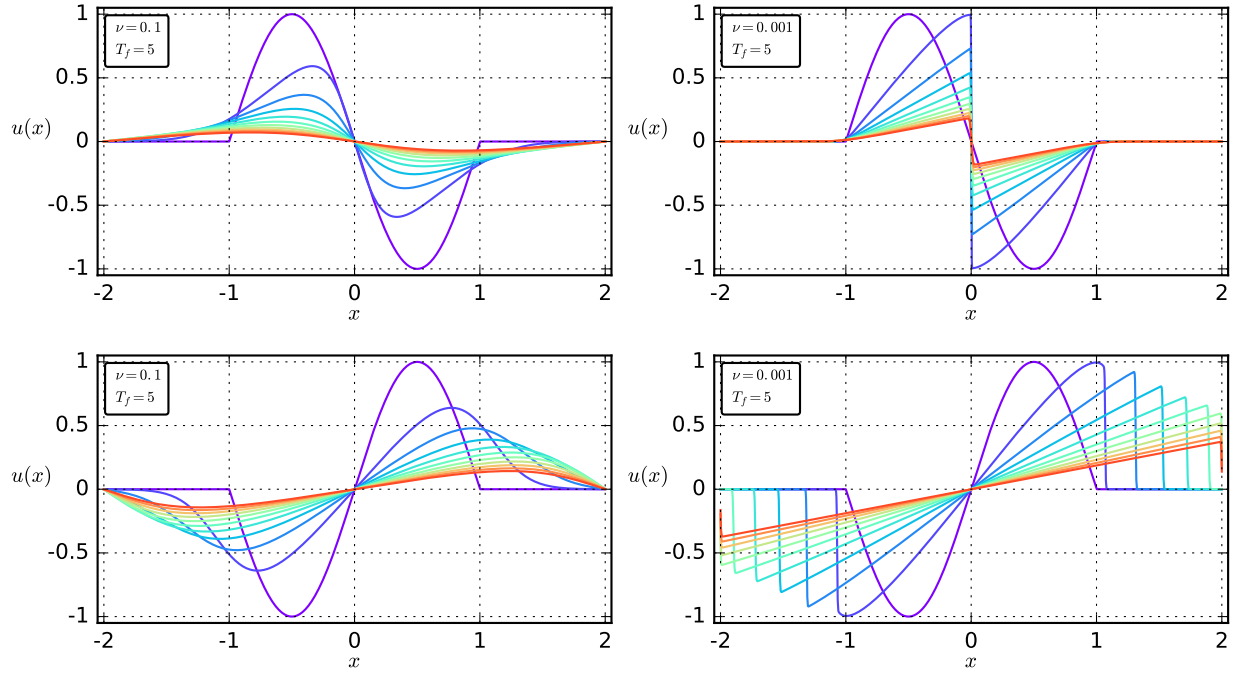


Figure 4: Simulations of the initial profile of the N-wave solution (top) and sine wave (bottom) for $\nu = 0.1$ and $\nu = 0.001$. Simulations were performed with 1600 steps ($\Delta x = 0.003$ and $\Delta t = 0.003$).

x	$u(x, T)$	U_j^T	$ u - U $
-0.5	0.999	0.999	0.000 076
-0.4	0.998	0.997	0.000 132
-0.3	0.995	0.995	0.000 215
-0.2	0.990	0.989	0.000 327
-0.1	0.979	0.979	0.000 455
0.0	0.960	0.959	0.000 553
0.1	0.925	0.924	0.000 522
0.2	0.865	0.865	0.000 213
0.3	0.774	0.774	0.000 445
0.4	0.648	0.649	0.001 138
0.5	0.500	0.501	0.001 110

Table 1: Results of a numerical simulation of Burgers' equation subject to Riemann initial conditions. Simulation was performed with 40 steps ($\Delta x = 0.1$ and $\Delta t = 0.025$), $\nu = 0.1$ and $T_f = 1.0$.

In table 1 the results of this simulation are shown. The simulation was performed using 40 time and spatial steps ($\Delta x = 0.1$ and $\Delta t = 0.025$) with viscosity set $\nu = 0.1$ and the final time, $T_f = 1.0$. These results capture the region where the gradient of the wave profile is most severe. One would expect that the simulation differ from the exact solution the most in this region. However the scheme seems to have performed well with the maximum absolute error in this region being around 1.0×10^{-3} . In figure (3) the numerical and exact solution are compared as well as displaying the evolution of the wave profile. The results shown here were performed with a finer grid, $\Delta x = 0.003$ and $\Delta t = 0.001$ and $T_f = 1.0$. We see that the numerical solution follows the exact solution almost exactly even for the small viscosity (bottom panel, $\nu = 0.001$). The effect of viscosity on the wave profile is also evident. The larger the viscosity the more energy is dissipated at either end of the shock (or wavefront) resulting in a smoother solution. When viscosity is low, we see the initial shock simply propagate forward, loosing little to no energy.

Figure 4 displays the evolution of sinusoidal initial wave profiles for various viscosity values. Here the waves have been fixed in the domain, $-1 \leq x \leq 1$, and outside this region has been set to zero. The boundary conditions for these simulations are $u(-2, t) = u(2, t) = 0$, with $T_f = 5$. The top panels show the initial profile of the N-wave solution,

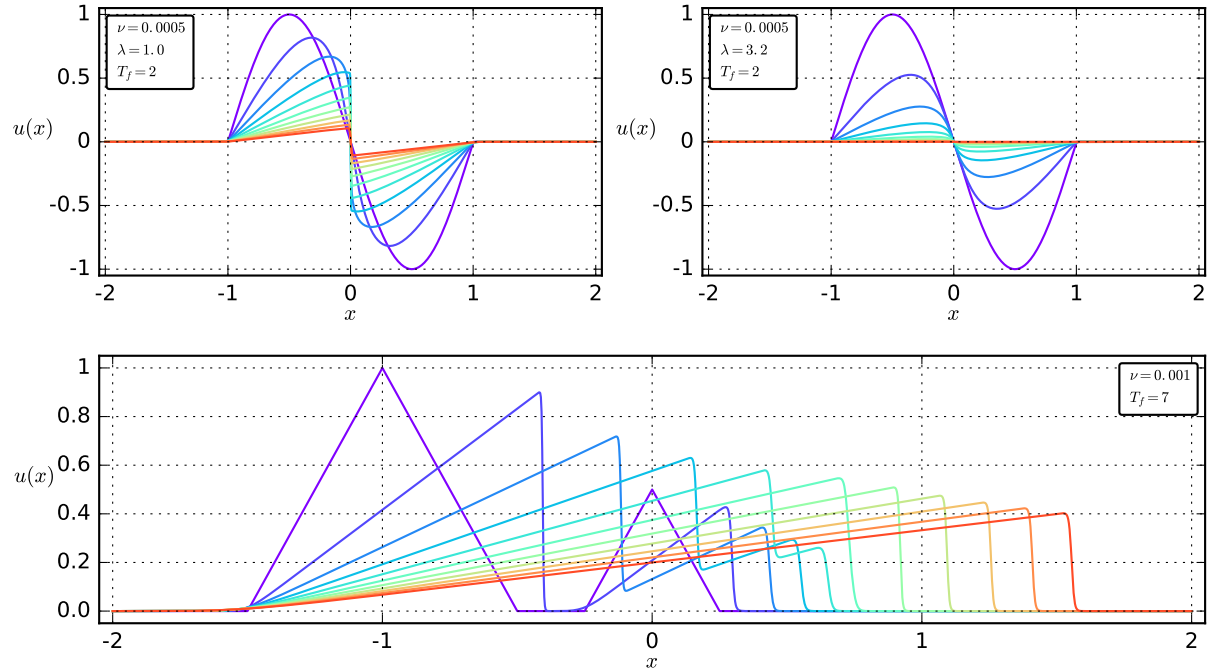


Figure 5: Simulation of initial wave profile of the N-wave solution (top) to investigate the effect of damping. Simulations were performed with 1600 steps ($\Delta x = 0.003$ and $\Delta t = 0.001$). (Bottom) Simulation of shock merger. Simulation was performed with 1600 steps ($\Delta x = 0.003$ and $\Delta t = 0.004$).

$u(x, 0) = -\sin(\pi x)$. We see that the pulses propagate toward the origin and for relatively large viscosity the pulses decrease in amplitude quite quickly, so much so that there is no evident shock formation. We also see the profile dissipate out at either side of the initial pulses i.e., $|x| > 1$. This is due to the effect viscosity has at smoothing the solution. This phenomena is not evident when viscosity is low, where in the top right panel we see the wave propagate towards the origin with the same initial amplitude until a shock forms and then the wave collapses. The bottom panels show a normal sine wave profile, $u(x, 0) = \sin(\pi x)$. We see the same effect of viscosity except this time the waves evolve away from the origin.

The top two panels in figure 5 show the effect of damping on the wave profile on the initial profile of the N-wave solution. Here we have set viscosity ($\nu = 0.0005$) very small in order to fully witness the damping. We saw in section 2.3 that the for a shock to form in such a situation $\lambda < \pi$. This is confirmed in the top left panel where we have set $\lambda = 1.0$. Although the amplitude decreases rapidly, shock formation still occurs. Where in the top left panel, with $\lambda = 3.2$ we see no shock formation, with the final wave collapsed entirely. The bottom panel in figure 5 displays the phenomena of shock confluence. This is achieved with the following initial conditions

$$u(x, 0) = \begin{cases} 2x + 3 & -\frac{3}{2} \leq x < -1, \\ -2x - 1 & -1 \leq x < -\frac{1}{2}, \\ 2x + \frac{1}{2} & -\frac{1}{2} \leq x < 0, \\ -2x + \frac{1}{2} & 0 \leq x \leq \frac{1}{4}. \end{cases} \quad (70)$$

Here we have set the pulse on the left to have larger initial amplitude than the right in order to for the pulse on the left to catch up with the right. We have also set viscosity to be low so that shocks can form. The simulation is run for $T_f = 7$ which gives enough time for the shocks to merge. We see that shocks form early on and then the shock on the left catch up with and eventually merge with the one on the right before it then propagates forward as a single wave. The phenomena of shock merging is important to work we discuss in the subsequent sections.

5 Triad Phase Dynamics in Fourier Space

In this section we turn our attention to the analysis of Burgers' equation in Fourier space. We follow closely the work carried out in [5] and particularly [13] where it is shown that triad phases play a key role in the dynamics of Burgers' equation in Fourier space. More

specifically, how the triad phases are crucial to the exchange and flux of energy in a Burgers' system. These papers examine a periodically forced version of Burgers' equation

$$\frac{\partial u}{\partial t} + \frac{1}{2} \frac{\partial u^2}{\partial x} = \nu \frac{\partial^2 u}{\partial x^2} + f(x, t), \quad (71)$$

on the domain $x \in [0, 2\pi]$, where $f(x, t)$ is the forcing injected into the system. We also provide visuals to show how the individual and triad phases organise in the lead up to and at triad phase synchronization events in the simulations performed in these papers. First, we discuss the formulation used in these papers.

5.1 Fourier Space Systems

In order to investigate the triad phase dynamics of (71) we must move from real space to Fourier space. Instead of the real velocity field $u(x, t)$, we concern ourselves with the Fourier modes (waves) $\hat{u}_k(t)$, such that

$$u(x, t) = \sum_{k=-\infty}^{\infty} \hat{u}_k(t) e^{ikx}, \quad (72)$$

where x is spatial position in real space and k is the wavenumber. We then perform a transformation of the form

$$\mathcal{F}[u(x, t)]_{k'} = \frac{1}{2\pi} \int_0^{2\pi} \left(\sum_{k=-\infty}^{\infty} \hat{u}_k(t) e^{ikx} \right) e^{-ik'x} dx, \quad (73)$$

to convert (71) to its Fourier space representation. Thus, Burgers' equation becomes

$$\frac{\partial \hat{u}_k}{\partial t} + \frac{1}{2} \mathcal{F} \left[\frac{\partial u^2}{\partial x} \right]_k = -\nu k^2 \hat{u}_k + \hat{f}_k, \quad (74)$$

where we have used the fact that $\mathcal{F} \left[\frac{d^n f(x)}{dx^n} \right] = (ik)^n F(k)$, where $F(k)$ is the Fourier transform of $f(x)$. The nonlinear term requires further manipulation and it is what produces the triad interactions

$$\begin{aligned}
\mathcal{F} \left[\frac{\partial u^2}{\partial x} \right]_k &= \mathcal{F} \left[\frac{\partial}{\partial x} \left(\sum_{k=-\infty}^{\infty} \hat{u}_k e^{ikx} \right)^2 \right]_k, \\
&= \mathcal{F} \left[\frac{\partial}{\partial x} \left(\sum_{k_1=-\infty}^{\infty} \hat{u}_{k_1} e^{ik_1 x} \right) \left(\sum_{k_2=-\infty}^{\infty} \hat{u}_{k_2} e^{ik_2 x} \right) \right]_k, \\
&= \mathcal{F} \left[\sum_{k_1=-\infty}^{\infty} \sum_{k_2=-\infty}^{\infty} \hat{u}_{k_1} \hat{u}_{k_2} \frac{\partial}{\partial x} e^{i(k_1+k_2)x} \right]_k, \\
&= \frac{1}{2\pi} \sum_{k_1=-\infty}^{\infty} \sum_{k_2=-\infty}^{\infty} i(k_1 + k_2) \hat{u}_{k_1} \hat{u}_{k_2} \int_0^{2\pi} e^{i(k_1+k_2-k)x} dx, \\
&= \sum_{k_1=-\infty}^{\infty} \sum_{k_2=-\infty}^{\infty} i(k_1 + k_2) \hat{u}_{k_1} \hat{u}_{k_2} \delta_{k_1, k_2}^k,
\end{aligned} \tag{75}$$

where we have used the integral representation of the Kronecker delta, δ_z^n , with $z = k_1 + k_2$ written as k_1, k_2 and $n = k'$. Substituting this back into (74) we find

$$\frac{\partial \hat{u}_k}{\partial t} = \frac{-ik}{2} \sum_{k_1, k_2 \in \mathbb{Z}} \hat{u}_{k_1} \hat{u}_{k_2} \delta_{k_1, k_2}^k - \nu k^2 \hat{u}_k + \hat{f}_k, \tag{76}$$

where we have dropped the prime on k for convenience. This ODE describes the evolution of Fourier modes over time under a Burgers' system. The convolution term dictates the dynamics of the Burgers' system, which manifests as interactions between modes that behave under the triad condition $k_1 + k_2 = k_3$.

In [5] it is shown that the phases of Fourier modes have a strong probability of taking a value of $\pi/2$ as well as having a tendency to cluster in and around this value for intermittent periods. This was achieved by investigating the evolution of the phase-amplitude representation of (76). By letting $\hat{u}_k(t) = a_k(t) e^{i\phi_k(t)}$ in the left and right hand side of (76) we can decompose the Fourier modes into their phase and amplitude representations

$$\begin{aligned}
\text{L.H.S.} &= \frac{\partial}{\partial t} a_k(t) e^{i\phi_k(t)}, \\
&= (\dot{a}_k + i\dot{\phi}_k a_k) e^{i\phi_k}, \\
\text{R.H.S.} &= \frac{-ik}{2} \sum_{k_1, k_2 \in \mathbb{Z}} a_{k_1}(t) a_{k_2}(t) e^{i(\phi_{k_1}(t) + \phi_{k_2}(t))} \delta_{k_1, k_2}^k - \nu k^2 a_k(t) e^{i\phi_k(t)} + \hat{f}_k, \\
&= \frac{-ik}{2} \sum_{k_1, k_2 \in \mathbb{Z}} a_{k_1} a_{k_2} e^{i(\phi_{k_1} + \phi_{k_2})} \delta_{k_1, k_2}^k - \nu k^2 a_k e^{i\phi_k} + \hat{f}_k, \\
\Rightarrow \dot{a}_k + i\dot{\phi}_k a_k &= \frac{-ik}{2} \sum_{k_1, k_2 \in \mathbb{Z}} a_{k_1} a_{k_2} e^{i(\phi_{k_1} + \phi_{k_2} - \phi_k)} \delta_{k_1, k_2}^k - \nu k^2 a_k e^{i(\phi_k - \phi_k)} + \hat{f}_k e^{-i\phi_k}.
\end{aligned}$$

Decomposing further into real and imaginary components we find a system of ODEs that describe the time evolution of the individual phase and amplitudes

$$\dot{a}_k = \frac{k}{2} \sum_{k_1, k_2 \in \mathbb{Z}} a_{k_1} a_{k_2} \sin(\varphi_{k_1, k_2}^k) \delta_{k_1, k_2}^k - \nu k^2 a_k + \Re(\hat{f}_k e^{-i\phi_k}), \quad (77)$$

$$\dot{\phi}_k = \frac{-k}{2} \sum_{k_1, k_2 \in \mathbb{Z}} \frac{a_{k_1} a_{k_2}}{a_k} \cos(\varphi_{k_1, k_2}^k) \delta_{k_1, k_2}^k + \frac{1}{a_k} \Im(\hat{f}_k e^{-i\phi_k}), \quad (78)$$

for a given wavenumber k , where $\varphi_{k_1, k_2}^k(t) = \phi_{k_1}(t) + \phi_{k_2}(t) - \phi_k(t)$ are the triad phases. We now have systems that describe how Burgers' equation evolves in Fourier space. In the next section we discuss tools used to investigate the role in which the triad phases play in the nonlinear dynamics of these systems, in particular we derive the result shown in [5] for the energy flux.

5.2 Energy Spectrum and Energy Flux

To study the effect triad phases have on the dynamics of the Fourier modes we examine the energy spectrum and in particular the energy flux across a wavenumber k . The definition of the flux of energy across a wavenumber k is as follows

$$\Pi(k, t) \equiv -\frac{1}{2} \frac{\partial}{\partial t} \left(\sum_{k'=-k}^k E_{k'}(t) \right), \quad (79)$$

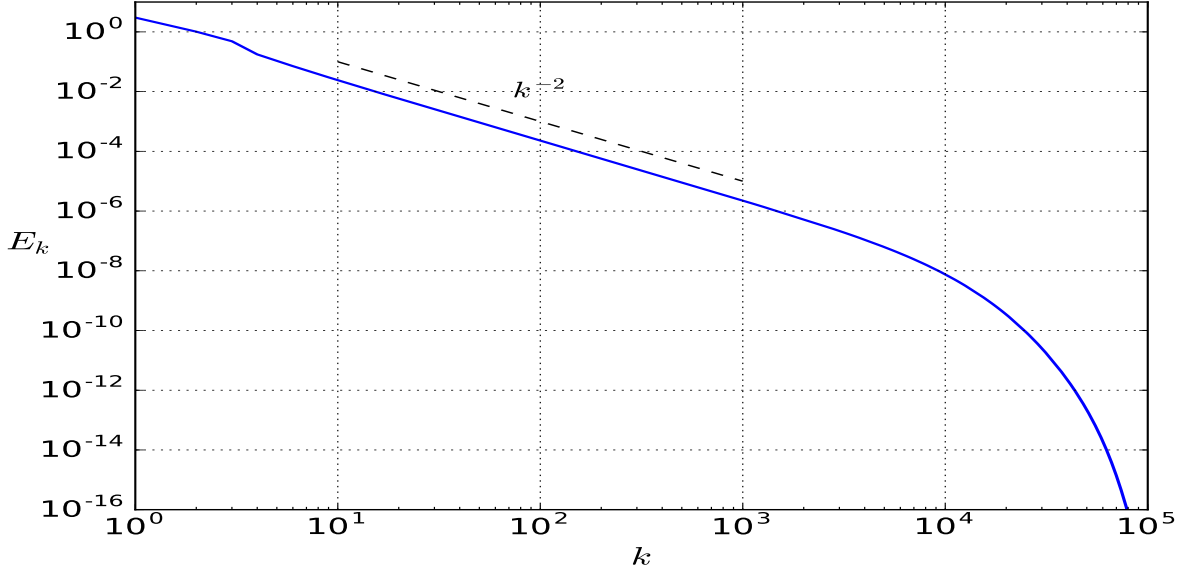


Figure 6: Time averaged energy spectrum for Burgers' equation exhibiting k^{-2} power-law decay in the inertial range.

where $E_k(t) = \hat{u}_k \hat{u}_k^*$ is the energy spectrum and \hat{u}_k^* is the complex conjugate of \hat{u}_k . The energy spectrum of Burgers' equation in the inertial range i.e., at scales away from excitation and dissipation, where nonlinear interactions dominate exhibit a decay $\propto k^{-2}$ (see figure 6). A spectrum with such scaling is the signature of a shock or shocks in Fourier space [2].

Applying the definition above to (76), and only concerning ourselves with the nonlinear terms we can find an expression for the energy flux up to a wavenumber k for our system. We first start by noticing that

$$\begin{aligned}
 \Pi(k) &= -\frac{1}{2} \frac{\partial}{\partial t} \left(\sum_{k'=-k}^k \hat{u}_{k'} \hat{u}_{k'}^* \right), \\
 \Pi(k) &= -\frac{1}{2} \sum_{k'=-k}^k \frac{\partial}{\partial t} (\hat{u}_{k'} \hat{u}_{k'}^*), \\
 \Pi(k) &= -\frac{1}{2} \sum_{k'=-k}^k \left(\frac{\partial \hat{u}_{k'}}{\partial t} \hat{u}_{k'}^* + \frac{\partial \hat{u}_{k'}^*}{\partial t} \hat{u}_{k'} \right). \tag{80}
 \end{aligned}$$

Therefore, by multiplying (76) by the complex conjugate of \hat{u}_k and ignoring the viscous and forcing terms, we get

$$\hat{u}_{k_1}^* \frac{\partial \hat{u}_{k_1}}{\partial t} = -\frac{ik_1}{2} \sum_{k_2, k_3 \in \mathbb{Z}} \hat{u}_{k_2} \hat{u}_{k_3} \hat{u}_{k_1}^* \delta_{k_2, k_3}^{k_1}, \quad (81)$$

where we have relabelled the wavenumbers k , k_1 and k_2 as k_1 , k_2 and k_3 respectively. Notice, however, we could have easily defined our equation in (76) in respect of its complex conjugate. So the equation above could have been written in conjugation form

$$\hat{u}_{k_1} \frac{\partial \hat{u}_{k_1}^*}{\partial t} = \frac{ik_1}{2} \sum_{k_2, k_3 \in \mathbb{Z}} \hat{u}_{k_2}^* \hat{u}_{k_3}^* \hat{u}_{k_1} \delta_{k_2, k_3}^{k_1}. \quad (82)$$

Substituting these two expressions back into (80) we get the following expression for the energy flux

$$\Pi(k) = \frac{i}{4} \sum_{|k_1| < k} \sum_{k_2, k_3 \in \mathbb{Z}} k_1 \left(\hat{u}_{k_2} \hat{u}_{k_3} \hat{u}_{k_1}^* - \hat{u}_{k_2}^* \hat{u}_{k_3}^* \hat{u}_{k_1} \right) \delta_{k_2, k_3}^{k_1}. \quad (83)$$

We can take advantage of the symmetry in the expression above, particularly in the k_1 variable. By replacing k_1 with $-k_1$ and using the fact that $\hat{u}_{-k}^* = \hat{u}_k$, we notice that the summation remains unchanged, however the expression now becomes

$$\Pi(k) = -\frac{i}{4} \sum_{|k_1| < k} \sum_{k_2, k_3 \in \mathbb{Z}} k_1 \left(\hat{u}_{k_1} \hat{u}_{k_2} \hat{u}_{k_3} - \hat{u}_{k_1}^* \hat{u}_{k_2}^* \hat{u}_{k_3}^* \right) \delta_{k_1, k_2, k_3}, \quad (84)$$

where we have the triad relation $k_1 + k_2 + k_3 = 0$. Like before, we can move to the phase-amplitude representation of the Fourier variables

$$\Pi(k) = \frac{1}{2} \sum_{|k_1| < k} \sum_{k_2, k_3 \in \mathbb{Z}} k_1 a_{k_1} a_{k_2} a_{k_3} \sin(\varphi_{k_1, k_2, k_3}) \delta_{k_1, k_2, k_3}, \quad (85)$$

where the triad phases are $\varphi_{k_1, k_2, k_3} = \phi_{k_1} + \phi_{k_2} + \phi_{k_3}$ and we have used the identity $\sin(\theta) = \frac{e^{i\theta} - e^{-i\theta}}{2i}$. Further examination of (85) and the triad condition would suggest that not all possible triads and triad phases are linearly independent. In fact, we can simplify our expression further by considering only the set of linearly independent triad phases. This set, along with the collection of the mode amplitudes, are what is defined as the ‘state space’ in [13] and [5].

Further reduction of (85) is achieved by taking advantage of the symmetries of the domains in which the wavenumbers k_1 , k_2 and k_3 lie, as well as considering only the possible

triad phases that can arise in these domains. Continuing in such a manner, we separate the summations of k_2 and k_3 into

$$\sum_{k_2 \in \mathbb{Z}} = \sum_{|k_2| < k} + \sum_{|k_2| > k} \quad (86)$$

$$\sum_{k_3 \in \mathbb{Z}} = \sum_{|k_3| < k} + \sum_{|k_3| > k}. \quad (87)$$

this results in a four termed expression for (85) in which three scenarios for producing triad phases are possible. The three cases are as follows: $\Pi_i(k)$, where all wavenumbers are inside $[-k, k]$; $\Pi_{ii}(k)$, where two wavenumbers are inside and one is outside $[-k, k]$ and $\Pi_{iii}(k)$, where one wavenumber (k_1) is inside $[-k, k]$ and the other two are outside.

Consider the first case for the moment

$$\Pi_i(k) = \frac{1}{2} \sum_{|k_1| < k} \sum_{|k_2| < k} \sum_{|k_3| < k} k_1 a_{k_1} a_{k_2} a_{k_3} \sin(\varphi_{k_1, k_2, k_3}) \delta_{k_1, k_2, k_3}, \quad (88)$$

where all wavenumbers are inside $[-k, k]$. We can again take advantage of the symmetries at our disposal, specifically we can transform $k_1 \rightarrow k_2$ and $k_1 \rightarrow k_3$. This produces three equally valid expressions for $\Pi_i(k)$ which we can take the average over. Noticing that the transformations have no effect on the form of the amplitudes, the $\sin(\varphi_{k_1, k_2, k_3})$, nor the summations, in fact the only change is to the factor of k_1 we find

$$\begin{aligned} \Pi_i(k) &= \frac{1}{3} \left(\frac{1}{2} \sum_{|k_1| < k} \sum_{|k_2| < k} \sum_{|k_3| < k} (k_1 + k_2 + k_3) a_{k_1} a_{k_2} a_{k_3} \sin(\varphi_{k_1, k_2, k_3}) \delta_{k_1, k_2, k_3} \right), \\ &= 0, \end{aligned} \quad (89)$$

which reduces to zero because of the triad condition $k_1 + k_2 + k_3 = 0$. This suggests that triad phases which arise in the region $[-k, k]$ conserve energy and have no contribution to the flux.

We now consider the case for $\Pi_{iii}(k)$, where one wavenumber k_1 , is inside $[-k, k]$ and the other two outside. The expression for this case is

$$\Pi_{iii}(k) = \frac{1}{2} \sum_{|k_1| < k} \sum_{|k_2| > k} \sum_{|k_3| > k} k_1 a_{k_1} a_{k_2} a_{k_3} \sin(\varphi_{k_1, k_2, k_3}) \delta_{k_1, k_2, k_3}. \quad (90)$$

Like before, we can split the summations for k_2 and k_3 into there positive and negative parts and consider the terms that are produced from the products of these cases. The only terms that satisfy the triad condition are those that have k_2 and k_3 on opposite sides of $[-k, k]$. That is, we ignore the terms where k_2 and k_3 are on the same side of $[-k, k]$

and consider only when k_2 is on the right and k_3 on the left of the interval and visa-versa. Therefore (90) becomes

$$\begin{aligned}\Pi_{iii}(k) &= \frac{1}{2} \sum_{|k_1| < k} \sum_{k_2 < -k} \sum_{k_3 > k} k_1 a_{k_1} a_{k_2} a_{k_3} \sin(\varphi_{k_1, k_2, k_3}) \delta_{k_1, k_2, k_3} \\ &\quad + \frac{1}{2} \sum_{|k_1| < k} \sum_{k_2 > k} \sum_{k_3 < -k} k_1 a_{k_1} a_{k_2} a_{k_3} \sin(\varphi_{k_1, k_2, k_3}) \delta_{k_1, k_2, k_3}.\end{aligned}\tag{91}$$

Taking the first term in the expression above and transforming k_1 and k_2 i.e., letting $k_1 \rightarrow -k_1$ and $k_2 \rightarrow -k_2$ and similarly letting $k_3 \rightarrow -k_3$ in the second term we find

$$\begin{aligned}\Pi_{iii}(k) &= \frac{1}{2} \sum_{|k_1| < k} \sum_{k_2 > k} \sum_{k_3 > k} (-k_1) a_{k_1} a_{k_2} a_{k_3} \sin(\varphi_{k_3}^{k_1, k_2}) \delta_{k_3}^{k_1, k_2} \\ &\quad + \frac{1}{2} \sum_{|k_1| < k} \sum_{k_2 > k} \sum_{k_3 > k} k_1 a_{k_1} a_{k_2} a_{k_3} \sin(\varphi_{k_1, k_2}^{k_3}) \delta_{k_1, k_2}^{k_3}, \\ &= \sum_{|k_1| < k} \sum_{k_2 > k} \sum_{k_3 > k} k_1 a_{k_1} a_{k_2} a_{k_3} \sin(\varphi_{k_1, k_2}^{k_3}) \delta_{k_1, k_2}^{k_3}.\end{aligned}\tag{92}$$

where we have used the fact that $\delta_{k_3}^{k_1, k_2}$ is the same as $\delta_{k_1, k_2}^{k_3}$ by definition and $\sin(\varphi_{k_3}^{k_1, k_2}) = \sin(-\varphi_{k_1, k_2}^{k_3}) = -\sin(\varphi_{k_1, k_2}^{k_3})$ with the triad condition $k_1 + k_2 - k_3 = 0$. We can further simplify the expression above by noticing the negation of the triad condition is also a valid triad i.e., $(-k_1) + (-k_2) - (+k_3) = 0$. This allows us to fold over the negative part of k_1 , or explicitly, split the k_1 summation into its negative and positive parts and by making the appropriate transformations in k_1, k_2 and k_3 we get

$$\Pi_{iii}(k) = 2 \sum_{k_1 > 0}^k \sum_{k_2 > k} \sum_{k_3 > k} k_1 a_{k_1} a_{k_2} a_{k_3} \sin(\varphi_{k_1, k_2}^{k_3}) \delta_{k_1, k_2}^{k_3}.\tag{93}$$

Finally, we make a further adjustment to the expression above by considering the restriction on the lower bound of k_3 . Since $k_1 \in [0, k]$, there is a minimum value k_3 can take in order for the triad condition of $k_1 + k_2 - k_3 = 0$ to be satisfied. By letting k_1 vary on the interval and substituting the minimum value for k_2 into the triad condition we find that the minimum value k_3 can take is $k_1 + (k + 1) = k_3$. Making this adjustment in k_3 and letting $k_2 = k_3 - k_1$ we drop the δ term to finally arrive at an expression for $\Pi_{iii}(k)$,

$$\Pi_{iii}(k) = 2 \sum_{k_1=1}^k \sum_{k_3=k_1+k+1}^{\infty} k_1 a_{k_1} a_{k_3-k_1} a_{k_3} \sin(\varphi_{k_1, k_3-k_1}^{k_3}).\tag{94}$$

Lastly, we consider $\Pi_{ii}(k)$, the case where two wavenumbers are inside the interval $[-k, k]$ and one outside. Since k_1 is restricted to the interval $[-k, k]$ there are only two possible ways to have two wavenumbers inside $[-k, k]$ i.e., k_2 inside with k_3 outside and visa-versa. Therefore we have

$$\begin{aligned}\Pi_{ii}(k) &= \frac{1}{2} \sum_{|k_1| < k} \sum_{|k_2| < k} \sum_{|k_3| > k} k_1 a_{k_1} a_{k_2} a_{k_3} \sin(\varphi_{k_1, k_2, k_3}) \delta_{k_1, k_2, k_3} \\ &\quad + \frac{1}{2} \sum_{|k_1| < k} \sum_{|k_2| > k} \sum_{|k_3| < k} k_1 a_{k_1} a_{k_2} a_{k_3} \sin(\varphi_{k_1, k_2, k_3}) \delta_{k_1, k_2, k_3}.\end{aligned}\quad (95)$$

Noticing the symmetry in k_2 and k_3 i.e., $k_1 + k_2 + k_3 = k_1 + k_3 + k_2 = 0$ we can swap k_2 and k_3 in the second term in the expression above to get

$$\Pi_{ii}(k) = \sum_{|k_1| < k} \sum_{|k_2| < k} \sum_{|k_3| > k} k_1 a_{k_1} a_{k_2} a_{k_3} \sin(\varphi_{k_1, k_2, k_3}) \delta_{k_1, k_2, k_3}.\quad (96)$$

We note that both k_1 and k_2 must be on the same side of the origin but the opposite side to k_3 in order to satisfy $k_1 + k_2 + k_3 = 0$ under the domains $|k_1|, |k_2| < k$ and $|k_3| > k$. Therefore considering these possibilities only we find

$$\begin{aligned}\Pi_{ii}(k) &= \sum_{k_1 > -k}^0 \sum_{k_2 > -k}^0 \sum_{k_3 > k} k_1 a_{k_1} a_{k_2} a_{k_3} \sin(\varphi_{k_1, k_2, k_3}) \delta_{k_1, k_2, k_3} \\ &\quad + \sum_{k_1 > 0}^k \sum_{k_2 > 0}^k \sum_{k_3 < -k} k_1 a_{k_1} a_{k_2} a_{k_3} \sin(\varphi_{k_1, k_3, k_2}) \delta_{k_1, k_3, k_2}.\end{aligned}\quad (97)$$

If we replace $k_1 \rightarrow -k_1$ and $k_2 \rightarrow -k_2$ in the first term and $k_3 \rightarrow -k_3$ in the second term we get

$$\begin{aligned}\Pi_{ii}(k) &= \sum_{k_1 > 0}^k \sum_{k_2 > 0}^k \sum_{k_3 > k} -k_1 a_{k_1} a_{k_2} a_{k_3} \sin(-\varphi_{k_1, k_2}^{k_3}) \delta_{k_1, k_2}^{k_3} \\ &\quad + \sum_{k_1 > 0}^k \sum_{k_2 > 0}^k \sum_{k_3 > k} k_1 a_{k_1} a_{k_2} a_{k_3} \sin(\varphi_{k_1, k_2}^{k_3}) \delta_{k_1, k_2}^{k_3}, \\ &= 2 \sum_{k_1 > 0}^k \sum_{k_2 > 0}^k \sum_{k_3 > k} k_1 a_{k_1} a_{k_2} a_{k_3} \sin(\varphi_{k_1, k_2}^{k_3}) \delta_{k_1, k_2}^{k_3}.\end{aligned}\quad (98)$$

Similar to the previous case, there is a restriction on k_3 under the triad condition of $k_1 + k_2 - k_3 = 0$. This time the maximum value k_3 can take depends on the restriction of k_1 and k_2 on the interval $[0, k]$. Like before, if we let k_1 vary and substitute in the maximum value k_2 can take, we find that the upper bound is $k_3 = k_1 + k$. Therefore (98) becomes

$$\Pi_{ii}(k) = 2 \sum_{k_1=1}^k \sum_{k_3=k+1}^{k+k_1} k_1 a_{k_1} a_{k_3-k_1} a_{k_3} \sin(\varphi_{k_1, k_3-k_1}^{k_3}). \quad (99)$$

where we have let $k_2 = k_3 - k_1$ in order to drop the δ term. We can now get a expression for the energy flux by pasting the summations on k_3 in the two terms for $\Pi_{ii}(k)$ and $\Pi_{iii}(k)$ together

$$\begin{aligned} \Pi(k) &= \Pi_{ii}(k) + \Pi_{iii}(k) \\ &= 2 \sum_{k_1=1}^k \left(\sum_{k_3=k+1}^{k+k_1} k_1 a_{k_1} a_{k_3-k_1} a_{k_3} \sin(\varphi_{k_1, k_3-k_1}^{k_3}) + \sum_{k_3=k_1+k+1}^{\infty} k_1 a_{k_1} a_{k_3-k_1} a_{k_3} \sin(\varphi_{k_1, k_3-k_1}^{k_3}) \right) \\ &= 2 \sum_{k_1=1}^k \sum_{k_3=k+1}^{\infty} k_1 a_{k_1} a_{k_3-k_1} a_{k_3} \sin(\varphi_{k_1, k_3-k_1}^{k_3}), \end{aligned} \quad (100)$$

where the triad phases are $\varphi_{k_1, k_3-k_1}^{k_3} = \phi_{k_1} + \phi_{k_3-k_1} - \phi_{k_3}$. The sign of the expression above and therefore the direction of the flux depend on the sign of $\sin(\varphi_{k_1, k_3-k_1}^{k_3})$ only, since all other terms in the expression are positive. If $\sin(\varphi_{k_1, k_3-k_1}^{k_3}) > 0$, then the contribution to the flux of energy in the system is positive and the direction is also positive producing a direct cascade of energy to small scale ranges. The flux is maximised when $\varphi_{k_1, k_3-k_1}^{k_3} = 2\pi + 2n\pi$ and in [5] it is shown that there is a strong tendency for the triad phases in the inertial range to cluster at and around this value.

5.3 Results

It was proposed in [13] that we use the Kuramoto model parameters to measure when triad phases synchronize and align to values of $\pi/2$ thus producing maximal energy exchanges. The Kuramoto model is used to model the synchronization of a system of coupled oscillators and the model parameters are defined as follows

$$\mathbf{R}e^{i\Phi} = \langle e^{i\varphi_{k_1, k_2}^{k_3}} \rangle_{k_1, k_2, k_3}, \quad (101)$$

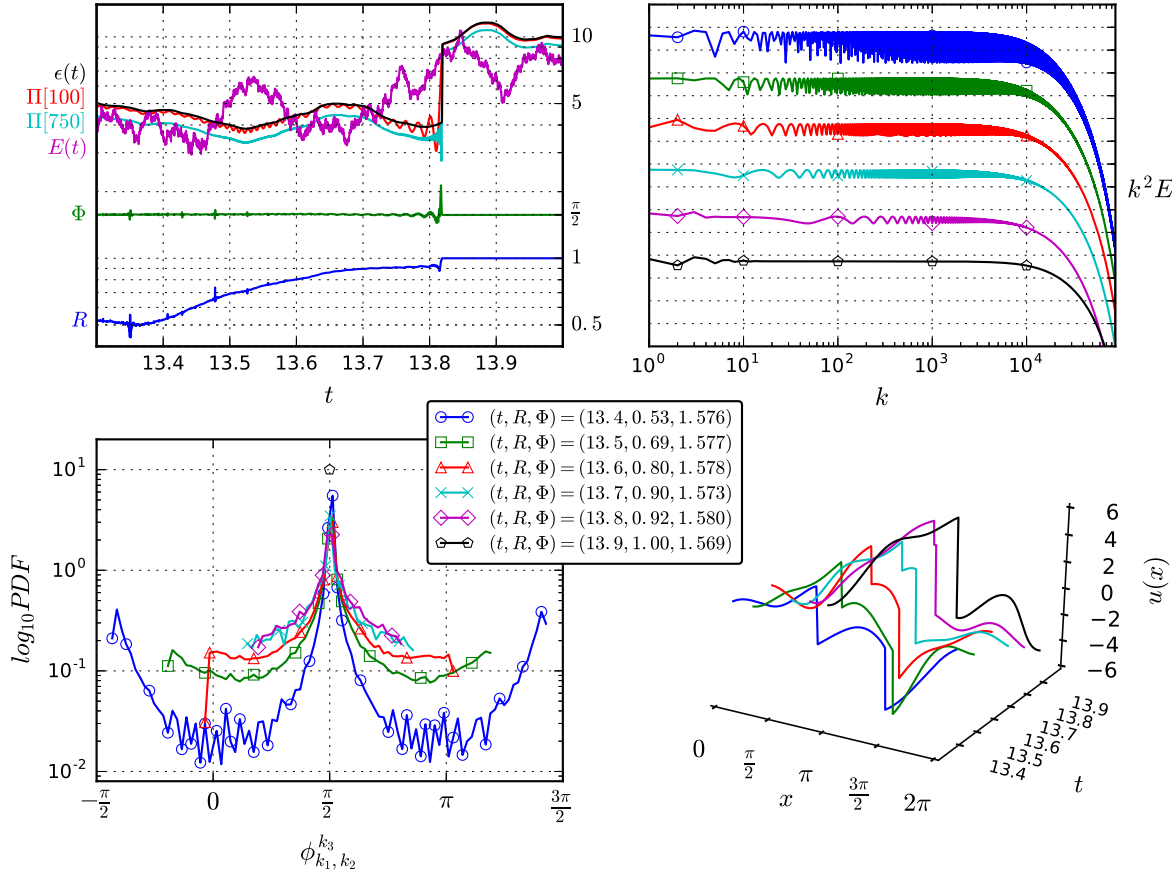


Figure 7: Snapshot ($t \in [13.3, 14.0]$) of the dynamics of a Burgers' system in lead up to a synchronization event. Top left panel shows the evolution of the synchronization and alignment parameters alongside the total energy in the system $E(t)$, the total dissipated energy $\epsilon(t)$ as well as the flux for $k = 100, 750$. The right panel shows the energy spectrum scaled by k^2 at six time points which have been shifted for visualization purposes. The bottom left panel displays the PDF for the triad phases in the inertial range $100 < k < 750$ ($\approx 160,000$ triads) for the six time points. The bottom right shows the real space solution for each of the six snapshots. Source: [13].

where $\langle \cdot \rangle_{k_1, k_2, k_3}$ denotes the average over all triads. The parameter $R(t)$ measures the synchronization of triad phases and takes a value $R(t) = 1$ when triad phases are synchronized i.e., when they take the same value. $R(t) = 0$ signifies when triad phases are completely desynchronized. Triad phase alignment to $\pi/2$ is measured by the $\Phi(t)$ parameter where $\Phi(t) \in [0, 2\pi]$. Murray and Bustamante, [13], show that these variables indicate intermittent periods of triad phase synchronization and alignment during simulations of (76) in their paper (for details of these simulations see paper).

Figure 7 displays the time evolution of these parameters as well as the system dynamics for a snapshot (in time) of the simulation in the lead up to a synchronization event. The top left panel shows the model parameters as well as the energy metrics for the system for this particular snapshot. The $R(t)$ parameter initially indicates that the system is desynchronized but as time advances the system becomes more synchronized until it reaches full synchronization ($R(t) = 1$) at $t \approx 13.8$. The $\Phi(t)$ parameter shows the triad phases oscillate around $\pi/2$ until they align exactly to $\pi/2$ at synchronization. The energy fluxes for the inertial range $\Pi(100)$ and $\Pi(750)$ show oscillations right before synchronization and then a sharp jump when triad phases synchronize and align producing maximal flux. There is a similar behaviour but without oscillation seen in the dissipation rate parameter $\epsilon(t)$, where $\epsilon(t) = 2\nu \sum_{k=1}^{\infty} k^2 E_k(t)$. Also shown is a measure for the total energy in the system $E(t)$, which is defined as $E(t) = \sum_{k=1}^{\infty} E_k(t)$, which shows no special behaviour other than fluctuations due to random forcing. The top right panel shows the energy spectrum, scaled by k^2 and shifted for visualization purposes, for six times (times indicated in the legend) during this snapshot. We see that when the system is desynchronized there are large fluctuations in the energy spectrum particularly across the inertial ranges where nonlinear interactions are dominant. But as the system approaches synchronization these fluctuations reduce until at synchronization we see the typical inertial range decay $\propto k^{-2}$. The bottom left panel shows the PDF of the triad phases in the inertial range for each of the six time points. Each of these PDFs show a large probability for triad phases to take values of $\pi/2$ even when out of synchronization. The PDFs show, that when the system is desynchronized, the triads phases take a wide range of values and exhibit leptokurtic behaviour, but as the system synchronizes the PDF ranges become smaller until at synchronization the PDF collapses to a single value of $\pi/2$, indicating that triad phases have completely aligned. Finally the bottom right panel shows a connection to shocks merging in real space where the real space solution for this period is shown. Initially there are two well defined shocks and as time progresses these shocks merge to form one large shock. This indicates that synchronization events correspond to shock mergers in real space.

In figure 8 we show a similar depiction to that of figure 7 with added visuals to show how the individual and triad phases organise in the lead up to such events of synchronization. The top left panel shows the solution in real space, where we have taken a snapshot of the simulation just as two shocks are about to merge. The top right panel displays the energy spectrum of the system at this point in time. The two panels below this show the model parameters (left) and the PDF of the triad phases (right) over the inertial range $25 < k < 1000$. The model parameters indicate that the system is currently at a stage of pre-synchronization and pre-alignment (red vertical line indicates current moment in the simulation). The PDF, centred at $\pi/2$, exhibits the same leptokurtic shape that we see in figure 7. The panel below displays the individual phases across the inertial range for this point in the simulation coloured according to the value they take, where $\phi_k \in [0, 2\pi]$. There is a somewhat obvious pattern to the individual phases, we see a banded or ordered

structure to the colouring of the phases and this banding is repeated across the range which is a result of the periodicity in ϕ_k . This banding of colour, although not perfect, would suggest that a linear relationship exists between ϕ_k and k for this particular snapshot. In fact, this linear relationship is important for the alignment and synchronization of triad phases. The only way all the triad phases can take the same value, except for the trivial case in which the individual phases are all the same value, is if the triad phases, the individual phases and k possess some simple linear relationship. This is evident in the bottom panel, where the triad phases in the inertial range (roughly 300,000 triads) are shown and coloured according to the value they take. We see that most triad phases for this snapshot have perfectly aligned and taken the value of $\pi/2$ (blue), this is reflected in the apparent linear relationship we see in ϕ_k and k . We also see clusters of triad phases with an organized structure taking values near to π (red) and zero (green).

We provide further examination of how the phases and triad phases organize in figure 9. We show the same visuals of the individual and triad phases shown in figure 8 but for three different points in the simulation. The top two panels show when the system is out of synchronization ($t = 4.067, R = 0.6, \Phi = 1.596$). The triad phases here are predominantly disorganized, although some do take values close to $\pi/2$. This disorganization is reflected in the individual phases where there is little to no banding structure apparent. The middle two panels refer to when the system is in the lead up to synchronization ($t = 4.512, R = 0.65, \Phi = 1.572$). We see the triad phases begin to organize with some having already aligned. The individual phases begin to exhibit a banded structure similar to that seen in figure 9, albeit with a much larger period. The triad phases also begin to form the clustered structures we saw in figure 9. These structures become larger as the system approaches synchronization. This can be seen in the bottom panel where system is just before complete synchronization ($t = 4.687, R = 0.75, \Phi = 1.6$). These structures have become much larger, similar in size to that seen in figure 9. It is not apparent in the figure, but these structures also propagate across the inertial range from left to right as the system tends to synchronization until at synchronization when these structures are no longer visible and the triad phases are completely aligned. The bottom panel also indicates that some triad phases have already aligned, this is reflected in the panel above where we see clear banding in the individual phases.

It is clear from figures 7 that the dynamics of the triad phases are critical in the evolution of a Burgers' system. In order to probe this further Murray and Bustamante also investigated a "phase only" model of Burgers' equation. This was achieved by fixing the amplitudes, a_k , and considering only the phase ODE in (78), of the phases-amplitude Burgers' model (for further details see paper). Similar results are observed; the phase only model experiences intermittent periods of synchronization with triad phases aligning to $\pi/2$. However there are some notable differences. In figure (10) we show a snapshot in the simulation of this phase-only model where the system is currently out of synchronization. The energy spectrum has been fixed (top right panel) and does not change throughout the simulation. As the system experiences no energy dynamics we see fluctuations in

the solution (top left panel) when the system is out of synchronization. However these fluctuations die out and we recapture the structured solution seen in the full model when the system becomes synchronized and aligned. The model parameters also vary more than the full model, with the $R(t)$ parameter taking values close to zero and the $\Phi(t)$ parameter experiencing larger oscillations. This is also reflected in the panel to the right where the PDF is more flat when out of synchronization. The clustered structures seen in the full model are no longer seen in the phase only model, instead we see the formation of linear structures in the lead up to synchronization. The individual phases also vary more, with the banded structure only apparent when the system is synchronized.

Figure 11 shows the individual phases and triad phases at three different points in the simulation. The top two panels refer to when the system is out of synchronization ($t = 4.855, R = 0.05, \Phi = 1.682$) where we see the individual and triad phases are completely disorganized. The next two panels show when the system is in the lead up to synchronization ($t = 5.539, R = 0.68, \Phi = 1.561$). The triad phases begin to organise with pockets having aligned or close to aligning already. We also see the development of linear structures in the triad phases. As the system approaches synchronization these structures flow across the inertial range, similar to the behaviour seen in the full model. The bottom panel, where the system is just before synchronization ($t = 5.703, R = 0.95, \Phi = 1.577$), shows these structures leaving the inertial range and the triad phases becoming aligned. Interestingly these structures are also reflected in the individual phases. Consider the linear structures in the regions near $k_3 = 620$ and $k_3 = 1000$ in the triad phases. These correspond to interruptions in the banded structure of ϕ_k in the panel above at around $k = 620$ and $k = 1000$. When the system is completely synchronized these structures leave the inertial range, similar to the full model, and the triad phases become completely aligned.

6 Conclusion

Burgers' equation possesses similar dynamical features to that of the Navier-Stokes equation. It is these dynamical features, such as the quadratic non-linearity, that we have discussed in this paper. We provided a derivation of the equation by seeking asymptotic solutions of a perturbed ideal gas using the method of multiple scales. We studied solutions to the inviscid case using the method of characteristics. We saw the characteristic curves to inviscid equation are straight lines with slope dependent on the velocity field u . This leads to the intersection of characteristics producing regions where the solution becomes multivalued. The point of intersecting characteristics is known as a shock and we discussed how to find the initial time and position of these shocks for various examples. The effect of damping on the dynamics of Burgers' equation was also discussed. It was shown that damping prevents the nonlinear distortion of the wave profile if $F'(\alpha) < -\lambda$, where λ is the positive damping parameter.

Through the Hopf-Cole transformation we saw that an exact solution to Burgers' equation exists and in the limit of vanishing viscosity we obtain the characteristic solution. We then used this exact solution as a benchmark to measure the accuracy of our numerical solutions. We implemented Crank-Nicolson with four-point upwind differencing to solve Burgers equation numerically for various initial wave profiles. Experimenting with the model parameters we explored the various features of Burgers' dynamics such as the effect the nonlinear term has at distorting the wave profile, resulting in shock formations in the solution. We also explored the effect viscosity has on the model, on how it smooths the solution and puts a structure on the shock.

Lastly we studied the dynamics of a periodically forced version of Burgers' equation in Fourier space. We discussed findings in recent work on the dynamics of triad phases, particularly the role they play in the energy exchanges in a Burgers' system. We saw that triad phases are crucial in the evolution of the phase-amplitude model of a Burgers' system in Fourier space as well as dictating the direction and magnitude of the energy fluxes across the scales. We saw that triad phases experience periods of synchronization and alignment to values of $\pi/2$, producing maximal energy fluxes towards small scales and that these synchronization events correspond to the merging of shocks in the real space solution. We also provided a visual examination on how the individual and triad phases organize in the lead up to synchronization events. The triad phase form organised non-trivial structures, particularly in the full Burgers' model, as the system approaches synchronization. These structures and their individual contributions to the flux may warrant further research, particularly in the full model case. In this paper did not provide a reasoning or give an understanding as to why these structures form and this may be another aspect that could be examined in the future.

Appendix

Extended Thomas Algorithm

The Thomas algorithm is a suitable tool for efficiently solving systems of linear equations of the form discussed in section 4. The algorithm was originally developed for tridiagonal systems [15] but can be easily extended to larger banded diagonal systems for example, pentadiagonal and in our case quadradiagonal systems. The algorithm involves reducing the coefficient matrix of the system to an upper triangular matrix (forward sweep) by eliminating the subdiagonal elements and then updating the super-diagonal elements. The system is then solved through backward substitution (backward sweep). In practice, to save computation and memory space, elimination of the subdiagonal elements is ignored and the super-diagonal elements are replaced by the corresponding updated elements. Below we present the extended Thomas algorithm for the pentadiagonal case.

The pentadiagonal linear system takes the form

$$A\mathbf{u} = \mathbf{d}, \quad (102)$$

where A is a $n \times n$ matrix, \mathbf{u} and \mathbf{d} are both $n \times 1$ length vectors given by

$$\begin{pmatrix} b_1 & c_1 & f_1 & & 0 \\ a_2 & b_2 & c_2 & \ddots & \\ e_3 & a_3 & b_3 & \ddots & f_{n-2} \\ \ddots & \ddots & \ddots & & c_{n-1} \\ 0 & & e_n & a_n & b_n \end{pmatrix} \begin{pmatrix} u_1 \\ u_2 \\ u_3 \\ \vdots \\ u_n \end{pmatrix} = \begin{pmatrix} d_1 \\ d_2 \\ d_3 \\ \vdots \\ d_n \end{pmatrix}. \quad (103)$$

The forward sweep consists of updating the super-diagonal elements as follows, where the prime denotes an updated element

$$\begin{aligned}
f'_i &= \frac{f_i}{\mu_i} & i = 1, 2, \dots, n-1, \\
c'_i &= \begin{cases} \frac{c_1}{\mu_1} & i = 1 \\ \frac{c_i - f'_{i-1}\gamma_i}{\mu_i} & i = 2, 3, \dots, n-1, \end{cases} \\
d'_i &= \begin{cases} \frac{d_1}{\mu_1} & i = 1 \\ \frac{d_2 - d'_1\gamma_2}{\mu_2} & i = 2 \\ \frac{d_i - d'_{i-2}e_i - d'_{i-1}\gamma_i}{\mu_i} & i = 3, 4, \dots, n, \end{cases} \tag{104}
\end{aligned}$$

where

$$\begin{aligned}
\gamma_i &= \begin{cases} a_1 & i = 2 \\ a_i - c'_{i-2}e_i & i = 3, 4, \dots, n, \end{cases} \\
\mu_i &= \begin{cases} b_1 & i = 1 \\ b_2 - c'_1\gamma_2 & i = 2 \\ b_i - c'_{i-1}\gamma_i - f'_{i-2}e_i & i = 3, 4, \dots, n. \end{cases} \tag{105}
\end{aligned}$$

The backward sweep produces the solution by carrying out the following

$$\begin{aligned}
u_n &= d'_n \\
u_{n-1} &= d'_{n-1} - c'_{n-1}u_n \\
u_i &= d'_i - c'_i u_{i+1} - f'_i u_{i+2} \quad i = n-2, n-3, \dots, 1. \tag{106}
\end{aligned}$$

The algorithm is a variant of Gaussian elimination that takes advantage of the band-edness and sparsity of A . It is therefore particularly economical; requiring only $\mathcal{O}(n)$ operations (multiplications and divisions) compared to that of $\mathcal{O}(n^3)$ for full Gaussian elimination. The algorithm in general is not stable but achieves stability for matrices that are symmetric positive definite or diagonally dominant i.e., $|b_i| > |a_i| + |c_i|$.

References

- [1] Bateman, H. (1915) 'Some recent researches on the motion of fluids', *Monthly Weather Review* 43, 163-170.
- [2] Bec, J. and Khanin, K. (2007) 'Burgers Turbulence', *Physics Reports*, 447(1-2), 1-66.
- [3] Billingham, J., King, A. C. (2000) *Wave Motion*, Cambridge University Press.
- [4] Burgers, J. M. (1948) 'A Mathematical Model Illustrating the Theory of Turbulence', *Advances in Applied Mechanics*, 1, 171-199.
- [5] Buzzicotti, M., Murray, B. P., Biferale, L. and Bustamante, M. D. (1948) 'Phase and precession evolution in the Burgers equation', *The European Physical Journal E*, 39(34).
- [6] Chowdhury, D. and Santen, L. (2000) 'Statistical Physics of Vehicular Traffic and Some Related Systems', *Physics Reports*, 329(199).
- [7] Cole, J. D. (1951) 'On a quasi-linear parabolic equation occurring in aerodynamics', *Quarterly of Applied Mathematics*, 9(3), 225-236.
- [8] Courant, R., Issacson, E. and Rees, M. (1952) 'On the solution of nonlinear hyperbolic differential equations by finite differences', *Communications on Pure and Applied Mathematics*, 5, 243-255.
- [9] Fay, R. D. (1931) 'Plane sound waves of finite amplitude', *The Journal of the Acoustical Society of America*, 3, 222.
- [10] Fletcher, C. A. J. (1988) *Computational Techniques for Fluid Dynamics*, Volume 1, Springer-Verlag, New York.
- [11] Hopf, E. (1950) 'The partial differential equation $u_t + uu_x = u_{xx}$ ', *Communications on Pure and Applied Mathematics*, 3(3), 201-230.
- [12] Kardar, M., Parisi, G. and Zhang, Y. C. (1986) 'Dynamical Scaling of Growth Interfaces', *Physical Review Letters*, 56(9), 889-892.
- [13] Murray, B. P. and Bustamante, M. D. (2017) 'Energy flux enhancement, intermittency and turbulence via Fourier triad phase dynamics in 1D Burgers equation', [arXiv:1705.08960 \[physics.flu-dyn\]](https://arxiv.org/abs/1705.08960) .
- [14] Nayfeh, A. H. (1993) *Introduction to Perturbation Techniques*, New York: John Wiley & Sons.

- [15] Thomas, L. H. (1949) ‘Elliptic Problems in Linear Differential Equations over a Network,’ Watson Science Computer Laboratory Report, Columbia University, New York.

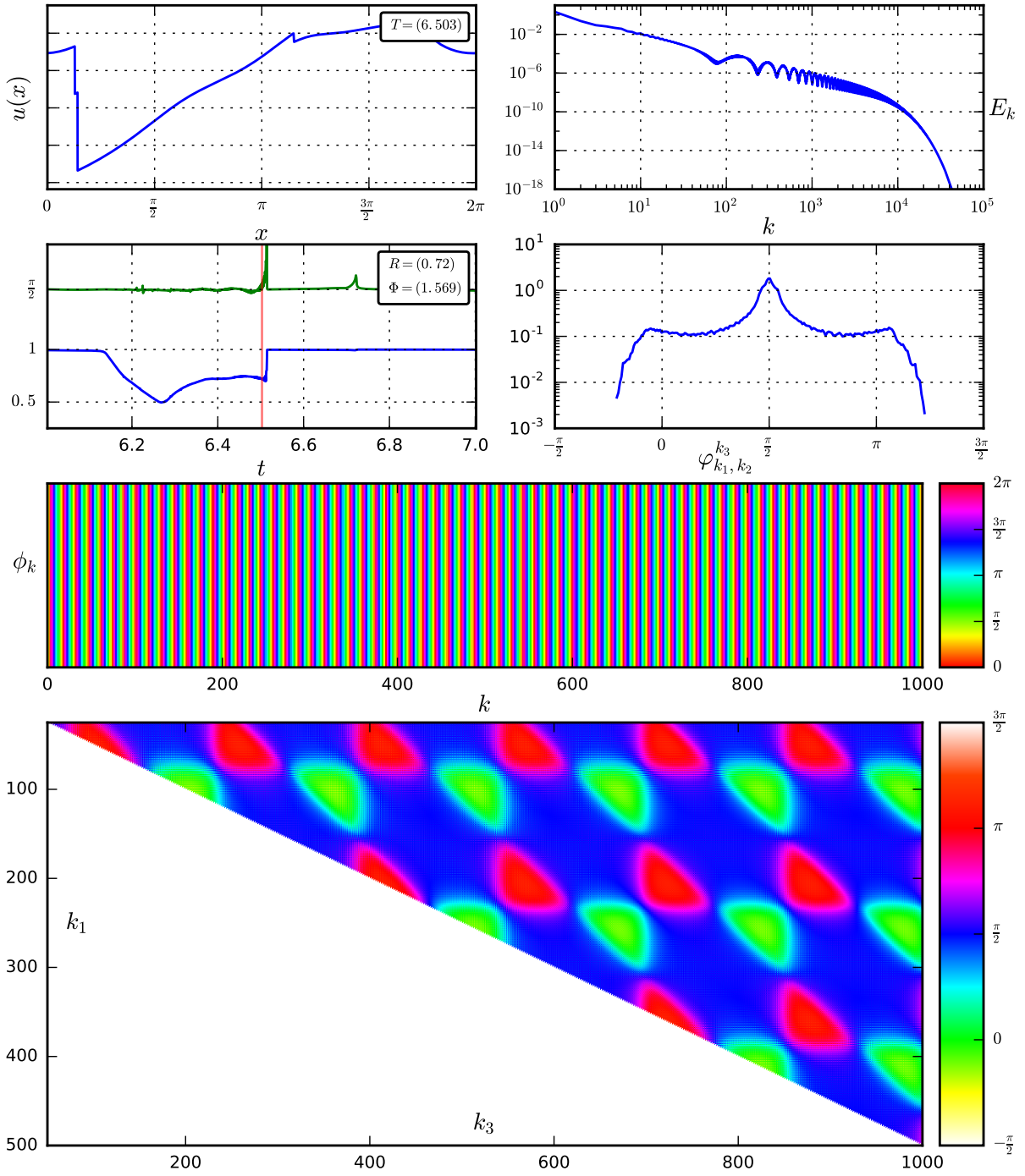


Figure 8: Snapshot of the system, individual phase and triad phase dynamics taken at $t = 6.503$ for the full Burgers' model in (76). For exact details of the simulations performed see [13].

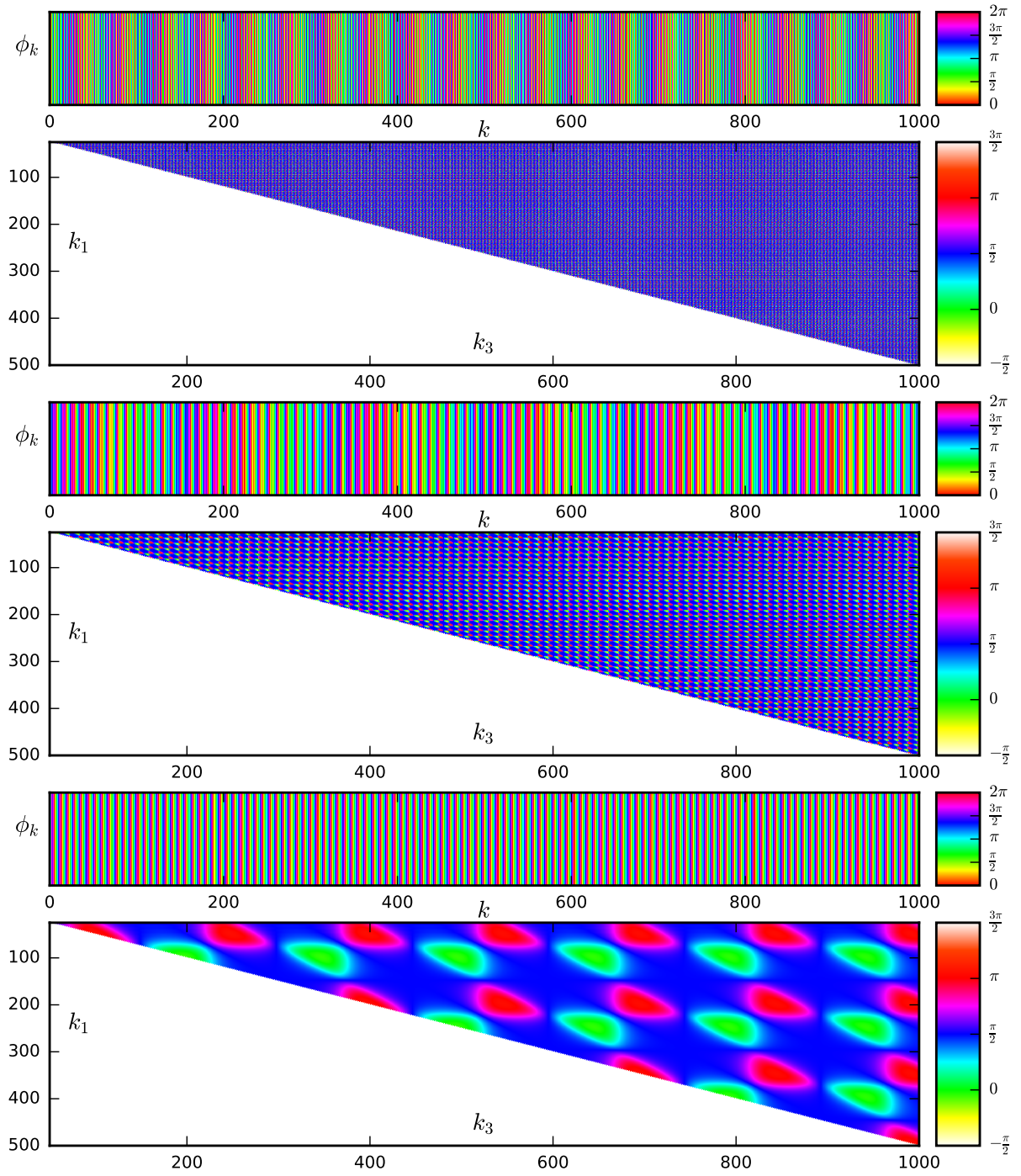


Figure 9: Snapshot of the individual phase and triad phase dynamics taken at $t = 4.067$ (top two panels), $t = 4.512$ (middle two panels) and $t = 4.687$ (bottom two panels) . For exact details of the simulations performed see [13].

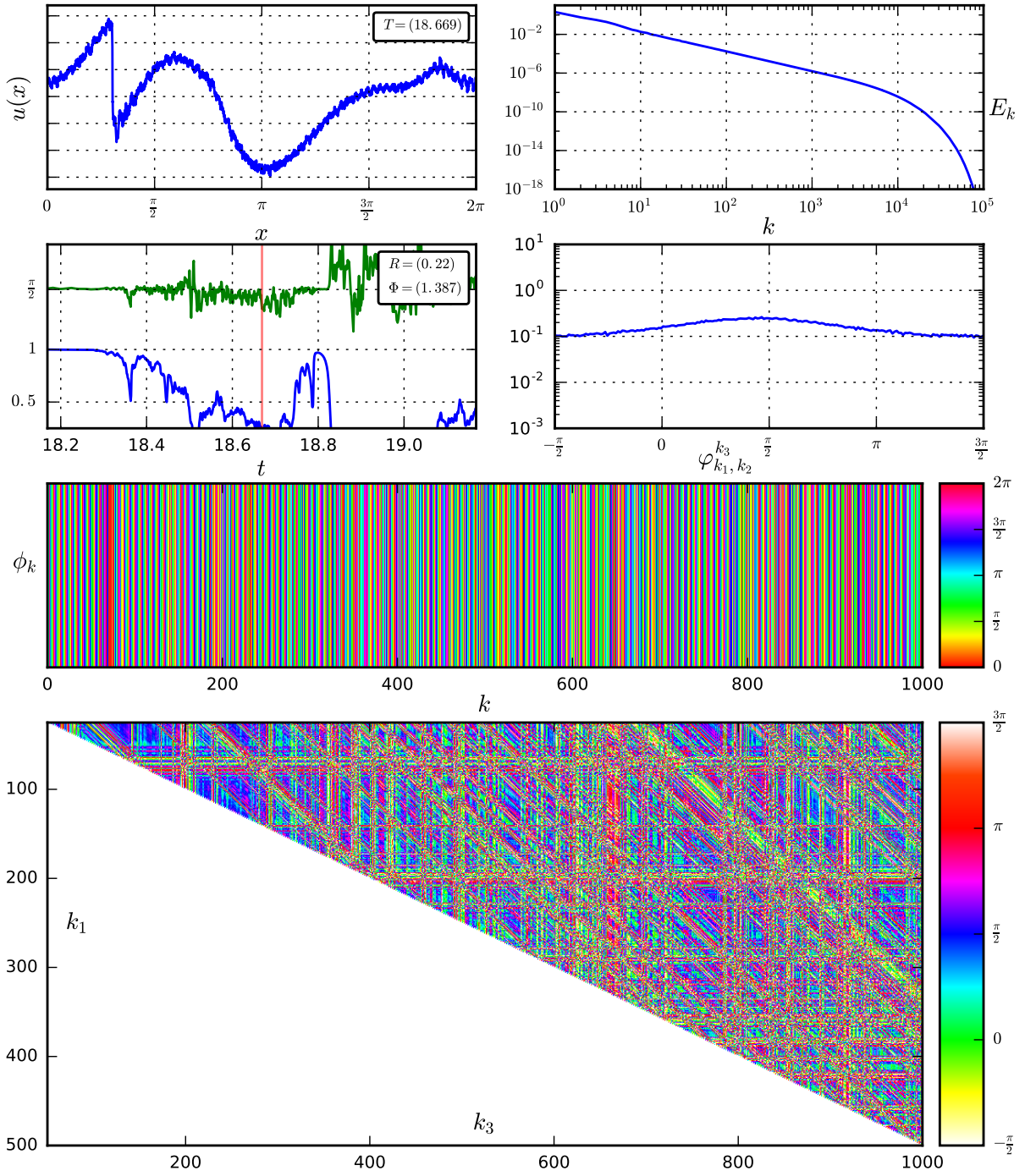


Figure 10: Snapshot of the system, individual phase and triad phase dynamics taken at $t = 18.669$ for the phase only Burgers' model in (78). For exact details of the simulations performed see [13].

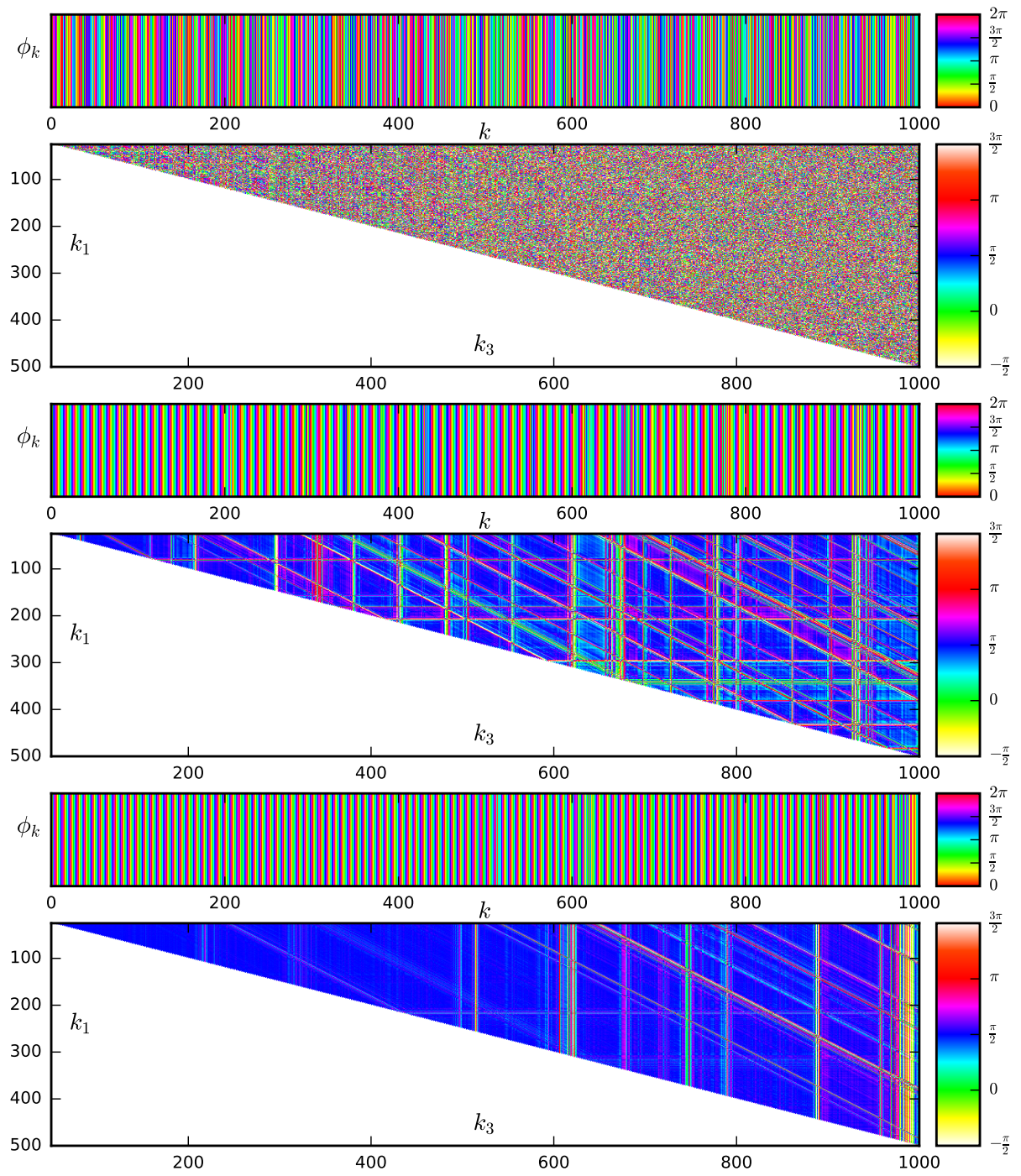


Figure 11: Snapshot of the individual phase and triad phase dynamics taken at $t = 4.855$ (top two panels), $t = 5.539$ (middle two panels) and $t = 5.703$ (bottom two panels). For exact details of the simulations performed see [13].